

HyDRo: Atmospheric Retrieval of Rocky Exoplanets in Thermal Emission

Anjali A. A. Piette,¹★ Nikku Madhusudhan,¹† Avi M. Mandell²

¹*Institute of Astronomy, University of Cambridge, Madingley Road, Cambridge, CB3 0HA, UK*

²*Solar System Exploration Division, NASA Goddard Space Flight Center, Greenbelt, MD 20771, USA*

Accepted XXX. Received YYY; in original form ZZZ

ABSTRACT

Emission spectroscopy is a promising technique to observe atmospheres of rocky exoplanets, probing both their chemistry and thermal profiles. We present HyDRo, an atmospheric retrieval framework for thermal emission spectra of rocky exoplanets. HyDRo does not make prior assumptions about the background atmospheric composition, and can therefore be used to interpret spectra of secondary atmospheres with unknown compositions. We use HyDRo to assess the chemical constraints which can be placed on rocky exoplanet atmospheres using JWST. Firstly, we identify the best currently-known rocky exoplanet candidates for spectroscopic observations in thermal emission with JWST, finding > 30 known rocky exoplanets whose thermal emission will be detectable by JWST/MIRI in fewer than 10 eclipses at $R \sim 10$. We then consider the observations required to characterise the atmospheres of three promising rocky exoplanets across the ~ 400 –800 K equilibrium temperature range: Trappist-1 b, GJ 1132 b, and LHS 3844 b. Considering a range of CO₂- to H₂O-rich atmospheric compositions, we find that as few as 8 eclipses of LHS 3844 b or GJ 1132 b with MIRI will be able to place important constraints on the chemical compositions of their atmospheres. This includes confident detections of CO₂ and H₂O in the case of a cloud-free CO₂-rich composition, besides ruling out a bare rock scenario. Similarly, 30 eclipses of Trappist-1 b with MIRI/LRS can allow detections of a cloud-free CO₂-rich or CO₂-H₂O atmosphere. HyDRo will allow important atmospheric constraints for rocky exoplanets using JWST observations, providing clues about their geochemical environments.

Key words: planets and satellites:atmospheres – planets and satellites:composition – infrared:planetary systems

1 INTRODUCTION

In recent years, the atmospheric characterisation of exoplanets has flourished, with increasingly detailed constraints made possible by unprecedented observations and sophisticated atmospheric retrieval tools and models (e.g. Crossfield 2015; Kreidberg 2018; Madhusudhan 2019). With the upcoming James Webb Space Telescope (JWST), the next frontier of atmospheric characterisation will turn towards smaller and cooler planets, including rocky exoplanets potentially hosting terrestrial-like secondary atmospheres (e.g. Greene et al. 2016; Lustig-Yaeger et al. 2019; Turbet et al. 2020). In this work, we report a new retrieval framework designed to analyse the thermal emission spectra of rocky exoplanets. We further use this framework to assess the ideal targets and observations needed to make important new constraints on rocky exoplanet atmospheric chemistry.

Recent observations have probed the atmospheres of several rocky exoplanets. For example, transmission spectroscopy of GJ 1132 b has suggested an atmosphere with a high-mean-molecular-weight (high- μ) and/or high-altitude clouds (Southworth et al. 2017; Diamond-Lowe et al. 2018; Mugnai et al. 2021). Similarly, transmission spectra of Trappist-1 d, e and f have ruled out clear, H₂-rich atmospheres for these planets (de Wit et al. 2018; Moran et al. 2018). Furthermore, searches for molecular species such as HCN have now become

possible in the atmospheres of rocky exoplanets such as 55 Cnc e and GJ 1132 b (Tsiaras et al. 2016; Swain et al. 2021; Mugnai et al. 2021) and could provide insights into their possible interior and atmospheric conditions (e.g. Madhusudhan et al. 2012).

Thermal phase curves have also been used to place constraints on rocky exoplanet atmospheres. The phase curve of 55 Cnc e displays a strong hot-spot shift, indicating the presence of an atmosphere (Demory et al. 2016; Hammond & Pierrehumbert 2017; Angelo & Hu 2017). In contrast, the strong day-night contrast and lack of hot-spot shift in the phase curve of LHS 3844 b suggests that this planet does not host a clear, H₂-rich atmosphere deeper than ~ 0.1 bar and may instead host a high-mean-molecular-weight and/or cloudy atmosphere, or no atmosphere at all (Kreidberg et al. 2019; Diamond-Lowe et al. 2020). Future observations, e.g. with JWST, will provide chemical constraints on rocky exoplanet atmospheres, leading to unprecedented constraints on their formation and evolution.

Thermal emission spectroscopy in particular offers an exceptional opportunity to characterise secondary, high- μ atmospheres on rocky exoplanets. This method is highly sensitive to atmospheric temperature profiles as well as molecular absorption. The mid-infrared wavelength range is particularly advantageous in the study of secondary atmospheres given the abundance of molecular features in this range (e.g. Deming et al. 2009; Greene et al. 2016; Madhusudhan 2019). Furthermore, the signal-to-noise ratio (S/N) achievable for secondary eclipse observations is maximised in the mid-infrared. JWST’s Mid-Infrared Instrument (MIRI), with a spectral range of ~ 5 –28 μm , will

★ E-mail: ap763@cam.ac.uk

† E-mail: nmadhu@ast.cam.ac.uk

therefore provide an unprecedented opportunity to investigate rocky exoplanet atmospheres including their chemical and thermal conditions.

Theoretical models of rocky planet atmospheres and surface-atmosphere interactions predict a wide range of possible atmospheric compositions beyond those seen in the solar system (Leconte et al. 2015). For example, surface-atmosphere interactions could result in atmospheres composed of H_2O , CO_2 , SO_2 , SiO , O_2 and H_2 depending on the surface conditions and bulk planetary properties (e.g. Gaillard & Scaillet 2014; Dorn et al. 2018; Herbort et al. 2020; Lichtenberg 2021; Schlichting & Young 2021). Degassing during accretion can further result in a wide range of atmospheric compositions including hydrogen, water and carbon compounds (Elkins-Tanton & Seager 2008). Furthermore, Hu et al. (2012) find that UV irradiation from an M-dwarf such as Trappist-1 could drive chemical reactions producing >1 bar of CO and/or O_2 . The interpretation of rocky exoplanet atmospheric observations therefore requires an approach which encompasses this chemical diversity.

Atmospheric retrievals have revolutionised atmospheric characterisation of exoplanets in the past decade (Madhusudhan 2018) and will be critical to provide detailed constraints on rocky exoplanet atmospheres. To date, retrievals of exoplanet emission spectra have typically been applied to hydrogen-rich atmospheres (e.g. Madhusudhan & Seager 2009, 2010; Lee et al. 2012; Line et al. 2013; Waldmann et al. 2015; Lavie et al. 2017; Gandhi & Madhusudhan 2018; Mollière et al. 2019) and do not consider secondary atmospheric compositions dominated by non-H species. However, Benneke & Seager (2012) report an agnostic chemical abundance parameterisation which does not assume a dominant atmospheric component a priori, and has been applied in the context of transmission spectroscopy (Benneke & Seager 2012, 2013; Welbanks & Madhusudhan 2021). By using the centred-log-ratio transformation, the parameterisation applies an identical prior probability distribution to each chemical species in the retrieval, allowing it to constrain the compositions of secondary atmospheres.

In this work, we present the first atmospheric retrieval framework for the thermal emission spectra of rocky exoplanets. The framework utilises the HYDRA emission retrieval framework of Gandhi & Madhusudhan (2018) and the chemical abundance parameterisation of Benneke & Seager (2012). It includes a range of opacity sources expected in secondary atmospheres, for example allowing for Venus-like and H_2O -dominated compositions. We further identify a large sample of optimal rocky exoplanet candidates for atmospheric characterisation in thermal emission with JWST MIRI. Focusing on three case studies, we use the new retrieval framework to investigate the chemical detections which can be made using JWST MIRI. In particular, we consider a hierarchy of science cases which can be used to systematically confirm/exclude increasingly complex atmospheric states.

In what follows, we describe the new retrieval framework in Section 2.1. In Section 2.2, we outline the self-consistent atmospheric model used to model rocky exoplanet thermal emission spectra, and use such a model in section 2.3 to validate the retrieval framework. We identify optimal rocky exoplanet candidates for atmospheric characterisation in Section 3. In Section 4, we investigate the observability of CO_2 and H_2O in three of the best targets for atmospheric characterization with MIRI in different temperature regimes: LHS 3844 b, GJ 1132 b and Trappist-1 b. We discuss further considerations in Section 5 and present our conclusions in Section 6.

Table 1. Prior probability distributions for the P - T profile parameters (see also Madhusudhan & Seager 2009, Gandhi & Madhusudhan 2018).

Parameter	Prior Distribution	Range
$\alpha_1/\text{K}^{-1/2}$	uniform	0.02 – 1
$\alpha_2/\text{K}^{-1/2}$	uniform	0.02 – 1
$T_{100\text{mb}}/\text{K}$	uniform	100 – 2500
P_1/bar	log-uniform	10^{-5} – 100
P_2/bar	log-uniform	10^{-5} – 100
P_3/bar	log-uniform	10^{-2} – 100

2 RETRIEVAL FRAMEWORK & ATMOSPHERIC MODEL

We describe here the HYDRA retrieval framework, adapted for use with rocky planets whose primary atmospheric constituent is unknown (Section 2.1). To test this framework and to provide predictions and observability strategies for JWST, we calculate self-consistent atmospheric models for known rocky exoplanets, and simulate their observed thermal emission spectra with JWST in Sections 2.3 and 4. These atmospheric models and simulated data are described in Section 2.2.

2.1 Retrieval Framework

In this work, we build on the HYDRA retrieval framework (Gandhi & Madhusudhan 2018) and adapt it for use with rocky exoplanets. HYDRA includes a parametric 1-D forward model coupled to a Nested Sampling Bayesian parameter estimation algorithm (Skilling 2006), PYMULTINEST (Feroz et al. 2009; Buchner et al. 2014). The inputs to the parametric forward model typically consist of a model pressure-temperature (P - T) profile and chemical abundances, which are used to calculate the emergent thermal emission spectrum of the planet. As in Gandhi & Madhusudhan (2018), we use the 6-parameter P - T profile of Madhusudhan & Seager (2009), which we find to be successful in retrieving the self-consistently derived temperature profiles of rocky exoplanets (Sections 2.3 and 4). The priors we use for each of the P - T profile parameters are shown in Table 1. These priors allow for both inverted and non-inverted temperature profiles in order to span the wide range of temperature gradients which can exist in the dayside atmosphere. As well as providing posterior probability distributions for the model parameters, the Nested Sampling algorithm further calculates the Bayesian evidence of the model fit. This can be used to perform robust model comparisons and to assess the statistical significance of molecular detections.

To date, HYDRA and adaptations thereof have been used to retrieve the thermal emission spectra of H_2 -dominated atmospheres, including hot Jupiters and brown dwarfs (Gandhi & Madhusudhan 2018; Gandhi et al. 2019; Piette & Madhusudhan 2020b). For these cases, the retrieval implicitly assumes that the background molecule is H_2 . In the case of rocky exoplanet atmospheres, however, the primary constituent of the atmosphere is unknown and a background molecule cannot be assumed. This motivates several adaptations to the retrieval framework, which are described in Sections 2.1.1 and 2.1.2 below. Unlike giant planets and brown dwarfs, rocky planets also have the potential to host little or no atmosphere at all due to atmospheric escape processes (e.g. Kreidberg et al. 2019). In Section 2.1.3, we discuss how the Bayesian evidences of rocky exoplanet retrievals can be used to statistically assess the presence of an atmosphere, as well as to calculate the detection significance for specific chemical species. We further validate the HYDRA retrieval framework in section 2.3 by applying it to simulated data for Trappist-1 b.

2.1.1 Chemical abundance parameterisation

In retrievals of H_2 -dominated atmospheres, the abundances of trace gases are typically included as parameters with a log-uniform prior. The mixing ratio of H_2 , X_{H_2} , is then calculated given the constraint that all mixing ratios, X_i , must sum to one, i.e.

$$\sum_{i=1}^n X_i = 1 \quad (1)$$

where n is the number of chemical species in the model. This treatment results in a different prior for the mixing ratio of the background molecule (in this case X_{H_2}) relative to the mixing ratios of the other species. This is shown in Figure 1; in particular, the prior for X_{H_2} is heavily skewed to higher values relative to the other chemical species. While appropriate for giant planets and brown dwarfs, these priors would result in biased results for low-mass exoplanets whose primary atmospheric constituent is unknown.

Benneke & Seager (2012) proposed an alternative parameterisation for the chemical mixing ratios in exoplanets with unknown dominant atmospheric constituents, and applied it to retrievals of transmission spectra of super-Earths. This parameterisation avoids the issues described above by using the centred-log-ratio (CLR) transformation, which is commonly used in the geological sciences to interpret compositional data (e.g. Pawlowsky-Glahn & Egozcue 2006). Here, we adopt this method for retrievals of thermal emission spectra. As described by Benneke & Seager (2012), the transformed ‘CLR’ parameters for each of the n chemical species included in the model, ξ_i , are given by

$$\xi_i = \ln \frac{X_i}{g(\mathbf{x})}, \quad (2)$$

where

$$g(\mathbf{x}) = \exp \left(\frac{1}{n} \sum_{i=1}^n \ln X_i \right). \quad (3)$$

The ξ_i parameters are then sampled by the Bayesian parameter estimation algorithm assuming uniform priors. In principle, ξ_i can vary between $-\infty$ and $+\infty$, corresponding to mixing ratios between 0 and 1. However, in practice, the chemical species have vanishing effects on the model spectrum once very small abundances are reached. For a given assumed minimum mixing ratio, p_{\min} , the corresponding maximum possible mixing ratio for a given species is $1 - p_{\min}(n - 1)$, following equation 1. For the ξ_i parameters, these limits translate to

$$\frac{1}{n} [\ln(p_{\min}) - \ln(1 - np_{\min})]$$

for the lower bound of the uniform prior, and

$$\frac{n-1}{n} [\ln(1 - np_{\min}) - \ln(p_{\min})]$$

for the upper bound. In this work, we choose to use $p_{\min} = 10^{-12}$, as in Benneke & Seager (2012). Once the ξ_i parameters have been sampled from this prior, they can be transformed back into mixing ratios (following equations 1, 2 and 3), and used to calculate the model spectrum:

$$X_i = \frac{e^{\xi_i}}{\sum_{j=1}^n e^{\xi_j}}.$$

The CLR parameterisation results in identical priors for the mixing ratios of each chemical species in the model, as shown in Figure 1. These priors are spiked towards higher abundances given the necessity that at least one species must have a large abundance (as noted

by Benneke & Seager 2012). The resulting parameter space therefore considers all chemical species in the model equally, allowing any of them to be the dominant atmospheric species.

2.1.2 Atmospheric opacity

Since rocky exoplanet atmospheres may be dominated by high mean-molecular-weight (high- μ) species, it is important to include all relevant sources of opacity for such species, including collision-induced absorption (CIA) and Rayleigh scattering. In our models, we therefore include the latest CO_2 - CO_2 and N_2 - N_2 CIA opacities from the HITRAN database (Karman et al. 2019), as well as H_2 - H_2 CIA opacity Richard et al. (2012). We further include Rayleigh scattering due to CO_2 , H_2O and H_2 (e.g. Malik et al. 2019). We note that the CIA data currently available is limited in temperature and wavelength. In this work, we therefore assume no CIA opacity outside the wavelength ranges available, and set the opacity at temperatures outside these limits to those at the boundary temperatures. Given the wide range of temperatures known for rocky exoplanets, future work will be required to more accurately assess the role of CIA opacity on their atmospheric spectra.

We also include molecular opacity due to species expected to be important in rocky exoplanet atmospheres which also have spectral features in the JWST/MIRI spectral range (~ 5 - $30 \mu m$), i.e. CO_2 , H_2O , CH_4 , O_2 , O_3 , and N_2 . These species are known to be important in the atmospheres of the solar system terrestrial planets and/or may dominate the atmospheres of rocky exoplanets in the temperature range considered here, i.e. $T_{eq} \sim 400 - 800 K$ (e.g. Herbot et al. 2020; Hu et al. 2020; Thompson et al. 2021; Wunderlich et al. 2021). While CO is also thought to be important in such atmospheres, it does not have significant features in the MIRI spectral range and we therefore exclude it from our present retrievals. In order to simulate a realistic, agnostic retrieval analysis, we include all of the opacity sources listed here in each of the retrievals in this work, regardless of the ‘true’ input composition.

The molecular cross sections for the species we include are calculated as described in Gandhi & Madhusudhan (2017) using line lists from the ExoMol, HITEMP and HITRAN databases (CO_2 and H_2O : Rothman et al. 2010, CH_4 : Yurchenko et al. 2013; Yurchenko & Tennyson 2014, O_2 and O_3 : Rothman et al. (2013), N_2 : Barklem & Collet 2016; Western et al. 2018). As discussed in Gandhi & Madhusudhan (2017), these cross sections are pressure broadened using the parameters for air broadening. Ideally, the pressure broadening would reflect the true composition of the atmosphere for each atmospheric model computed in the retrieval. However, given the wide range of possible atmospheric compositions for rocky exoplanets, this approach would be very cumbersome (e.g. Scheucher et al. 2020) and computationally expensive in the context of an atmospheric retrieval, in which a wide range of compositions is explored. Furthermore, the relevant line broadening coefficients are not all currently known (e.g. Fortney et al. 2019). Further work on the pressure broadening of molecular opacities in rocky exoplanet atmospheres will be needed in order to improve these models and retrievals in the future.

Figure 2 shows the molecular opacities included in the retrieval as a function of wavelength, as well as the spectral coverage of JWST/MIRI’s Low Resolution Spectroscopy (LRS) mode and F1500W photometric band. Some species have overlapping molecular absorption in the MIRI spectral range and may potentially lead to degeneracies in the retrieved abundances, depending on the data quality and spectral coverage. For example, H_2O and CH_4 have a somewhat similar cross section profile in the MIRI LRS spectral range. Similarly, CO_2 and O_3 both have strong features at $\sim 9 \mu m$. In

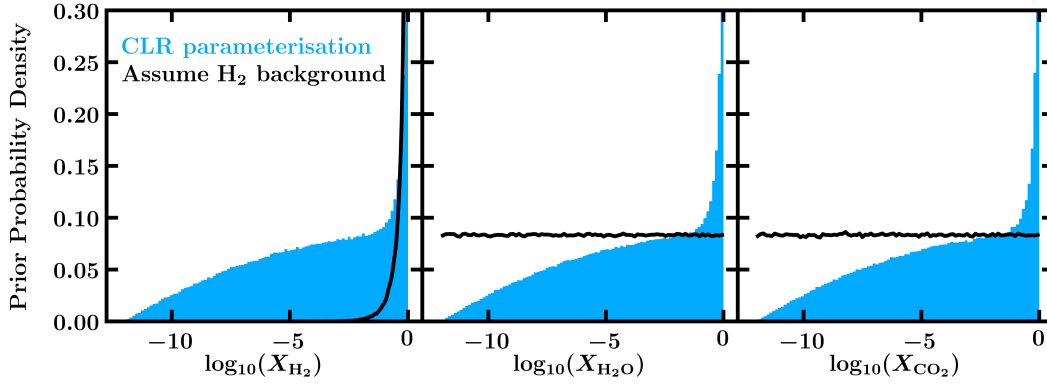


Figure 1. Prior probability densities for log chemical abundances using the centred-log-ratio (CLR) parameterisation (blue) or assuming a H_2 -dominated composition and log-normal priors for the other species (black). The CLR parameterisation results in identical priors for all species, without assuming a fixed background species.

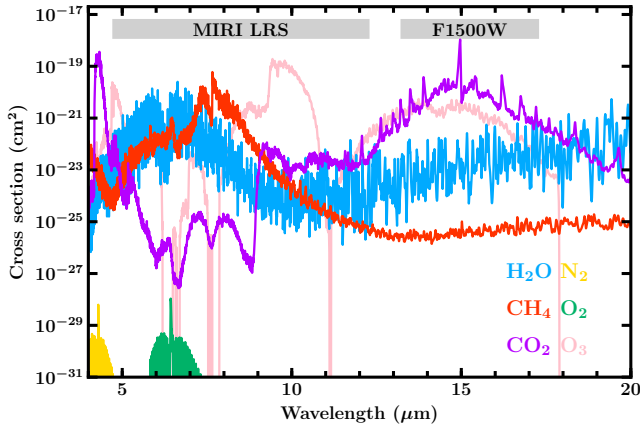


Figure 2. Key sources of opacity in the mid-infrared for secondary atmospheres, at a pressure of 1 bar and temperature of 500 K. The wavelength ranges of MIRI LRS and the MIRI F1500W photometric band are shown by thick grey lines.

section 4, we consider atmospheric compositions ranging from CO_2 -rich to H_2 -O-rich, and find that H_2O and CO_2 can both be detected in the thermal emission spectrum despite these degeneracies.

2.1.3 Atmospheric detections

The Bayesian evidence of a retrieved model fit can be used to statistically and robustly compare different retrieval models (e.g. Trotta 2008). The Nested Sampling algorithm used in `HYDRO` calculates the Bayesian evidence of the retrieved model fit and therefore allows such comparisons to be made. Bayesian model comparison is commonly used to assess the statistical significance of molecular detections by comparing retrieval models which include/exclude a certain molecule (e.g. Benneke & Seager 2013; Gandhi & Madhusudhan 2018). Here, we consider how such model comparison can be used to assess the presence of an atmosphere or specific molecules by comparing models with/without the presence of molecular features.

For two different retrieval models, a and b , the ratio of their Bayesian evidences (i.e. the Bayes factor),

$$\mathcal{B}_{a,b} = \frac{p(\text{data}|\text{model } a)}{p(\text{data}|\text{model } b)},$$

provides a measure of how likely model a is relative to model b . For example, $\ln(\mathcal{B}_{a,b}) = 1.0, 2.5$ or 5.0 suggests weak, modest and strong evidence for model a over model b , respectively (Trotta 2008). The Bayes factor can further be converted to a ‘sigma’ value to represent the confidence of the detection Benneke & Seager (2013). The comparison of Bayes factors can be used to evaluate the significance of specific molecular detections (e.g. Benneke & Seager 2013; Gandhi & Madhusudhan 2018). To do this, a retrieval which includes all model parameters is compared to a model which includes all model parameters apart from the abundance of the molecule in question.

The presence of an atmosphere on a transiting exoplanet can be inferred in several ways (e.g. Koll et al. 2019; Mansfield et al. 2019), including the detection of absorption features in its thermal emission spectrum. In order to calculate the significance of such an atmospheric detection, we compare each of our retrievals in Sections 2.3 and 4 to a featureless blackbody retrieval model, whose only parameter is the surface temperature. The resulting Bayes factor therefore indicates the confidence with which atmospheric absorption is detected. We note that surface reflection may lead to a bare planet having spectral features despite the lack of an atmosphere (e.g. Hu et al. 2012). However, such features are typically expected to be small; comparison to a blackbody spectrum thus provides a good first-order estimate of whether an atmosphere is present.

2.2 Self-Consistent Atmospheric Model & Simulated Data

In order to test the observability of known rocky exoplanets, we first use self-consistent 1-D atmospheric models to simulate their thermal emission spectra and then use `HYDRO` to assess the observations needed for robust chemical detections. We use an adaptation of the `GENESIS` self-consistent atmospheric model (Gandhi & Madhusudhan 2017; Piette et al. 2020; Piette & Madhusudhan 2020a) to do this. `GENESIS` self-consistently solves radiative-convective, hydrostatic and thermochemical equilibrium to find the steady-state P - T profile and thermal emission spectrum of the atmosphere. We use direct, second-order methods to solve the equation of radiative transfer; as described in Piette & Madhusudhan (2020a), we use the Feautrier method (Feautrier 1964) in the iterative solution of radiative-convective equilibrium, and the Discontinuous Finite Element method (Castor et al. 1992) combined with Accelerated Lambda Iteration for the final calculation of the spectrum.

At the base of the atmosphere, we assume a surface pressure of 10 bar and a small internal flux corresponding to an internal tempera-

ture of 10 K, i.e. somewhat comparable to the internal temperatures of the terrestrial planets in the solar system (e.g. Zharkov 1983; Davies & Davies 2010; Parro et al. 2017). We note that in the retrievals shown in sections 2.3 and 4, we assume a fixed surface pressure equal to that used here to generate the simulated data (i.e. 10 bar). The retrieval is not sensitive to the choice of surface pressure, as long as it is deep enough to encompass the photosphere. We demonstrate this in Appendix A for the validation retrieval of Trappist-1 b shown in Section 2.3.

We model the stellar irradiation for GJ 1132 b using a Kurucz stellar model (Kurucz 1979; Castelli & Kurucz 2003) corresponding to the stellar properties listed in Table 2. For the stellar spectra of Trappist-1 and LHS 3844, however, we use PHOENIX models (Husser et al. 2013) as their effective temperatures (~ 2500 K and ~ 3000 K, respectively) are significantly below the coolest temperature considered in the Kurucz models (3500 K). We further assume full day-night energy redistribution, i.e. a flux redistribution factor of $f=0.25$ according to the notation of Burrows et al. (2008).

In section 4, we focus on three key atmospheric compositions ranging from CO_2 -rich to H_2O rich. These are: (i) a Venus-like composition with 97% CO_2 , 2.9% N_2 and 0.1% H_2O by volume, (ii) a 50% CO_2 , 50% H_2O composition (by volume) and (iii) a 100% H_2O composition. We include molecular opacity from each of these species as well as CO_2 - CO_2 and N_2 - N_2 CIA, and Rayleigh scattering due to CO_2 and H_2O (see Section 2.1.2). For simplicity, we assume constant-with-depth chemical abundances. We note that a range of other species (e.g. NH_3 , HCN , SO_2 or H_2S) may also be present in rocky exoplanet atmospheres, for example due to photochemistry or outgassing (e.g. Moses 2014; Herbort et al. 2020; Thompson et al. 2021; Wunderlich et al. 2021; Yu et al. 2021). However, for simplicity we focus here on $\text{CO}_2/\text{H}_2\text{O}$ -dominated compositions. For each of the planets modelled in Sections 2.3 and 4, we list the planetary and stellar parameters used in Table 2.

From the model thermal emission spectra calculated using GENESIS, we simulate both MIRI LRS spectra and MIRI photometry. For the MIRI LRS spectra, we bin the model spectrum to the pixel resolution and convolve it to a resolution of $R \sim 100$ (i.e. close to the instrument resolution) using a Gaussian kernel. The Gaussian kernel has fixed full width at half maximum (FWHM), chosen such that $\text{FWHM} = \lambda/100$ at the centre of the MIRI LRS spectral range, i.e. at $\lambda = 8.5 \mu\text{m}$. We calculate the uncertainties on the simulated LRS data using PANDEMO (Batalha et al. 2017) using a noise floor of 20 ppm at native resolution, and add this as random Gaussian noise to the simulated data. For the simulated MIRI photometry, we bin the spectra using the instrument response functions for each band (Glasse et al. 2015) and assume nominal single-eclipse uncertainties of 100 ppm, i.e. a conservative estimate of the uncertainties expected for the targets considered in section 4 (e.g. Lustig-Yaeger et al. 2019). As with the simulated MIRI LRS data, we add this uncertainty as random Gaussian noise to the simulated photometry data. In this work, we use the F1500W photometric band at $\sim 15 \mu\text{m}$ as this probes opacity due to CO_2 and H_2O , as shown in Figure 2.

2.3 Validation of Retrieval Framework

We validate the retrieval framework by applying it to simulated data for Trappist-1 b. We further compare our results to Lustig-Yaeger et al. (2019), who have assessed the atmospheric observability of the Trappist-1 planets. We model the spectrum of Trappist-1 b assuming a Venus-like composition and simulate its MIRI LRS spectrum, as described in Section 2.2. We simulate data uncertainties assuming 30 eclipses. The self-consistent temperature profile and thermal

emission spectrum obtained (including simulated data) are shown in Figure 3. Note that the simulated MIRI LRS data shown in Figure 3 have been binned for clarity, but the data used for the retrieval are at the native resolution.

The retrieved spectrum and temperature profile are also shown in Figure 3, alongside the posterior distributions for the chemical abundances in the model. 2D marginalised posterior probability distributions are shown in Appendix B. Both CO_2 and H_2O (the only spectrally active species in the self-consistent model) are detected with strong statistical confidence, at 5.51σ and 4.90σ , respectively. Correspondingly, the retrieved spectrum is able to fit the CO_2 absorption feature at $\sim 9 \mu\text{m}$ as well as the broad absorption feature due to H_2O around $\sim 6 \mu\text{m}$. This result is consistent with Lustig-Yaeger et al. (2019), who find that ~ 30 eclipses with MIRI LRS are able to significantly rule out a featureless emission spectrum for Trappist-1 b, in the case of a clear 10 bar CO_2 atmosphere.

We further find that the retrieval is able to accurately fit the photospheric temperature profile with very good precision, within $\lesssim 200$ K at 2σ . The retrieved P - T profile in Figure 3 is able to reproduce the ‘true’ input temperature profile to within 2σ throughout the atmosphere, with a tighter fit at photospheric pressures and larger uncertainty outside the photospheric range (as expected, since these regions have little effect on the observable spectrum). Thermal emission observations of rocky exoplanets therefore have the potential to place exquisite constraints on the thermodynamic conditions in their atmospheres.

3 TARGET SELECTION

In this Section, we evaluate the observability of known rocky exoplanets in thermal emission, and identify optimal candidates for atmospheric characterisation. Since the planet-star contrast is greater at longer wavelengths, we specifically assess the planets’ observability in the mid-infrared with MIRI LRS, i.e. in the spectral range $5\text{--}12 \mu\text{m}$. We begin by considering all known exoplanets in the NASA Exoplanet Archive¹ with masses $< 10M_\oplus$ and radii $< 2R_\oplus$ whose stars have K magnitudes < 13 . We further include LHS 3844 b, which does not have a measured mass but represents an ideal target for rocky exoplanet characterisation.

In order to identify optimal targets for thermal emission observations, we first assess these targets by considering their planetary and stellar spectra to be blackbodies. For the planetary temperature, we calculate the equilibrium temperature of the planet assuming zero albedo and full day-night energy redistribution, i.e.

$$T_p = \sqrt{\frac{R_s}{2a}} T_{\text{eff}},$$

where R_s and T_{eff} are the stellar radius and effective temperature, respectively, and a is the semi-major axis. We then calculate the planet-star flux ratio for each system,

$$\frac{F_p}{F_s} = \frac{R_p^2 B_\lambda(T_p)}{R_s^2 B_\lambda(T_{\text{eff}})},$$

where R_p is the planetary radius and B_λ is the Planck function. We filter the targets according to F_p/F_s in three steps:

- (i) Filter out any targets for which $F_p/F_s < 10$ ppm at $12 \mu\text{m}$

¹ exoplanetarchive.ipac.caltech.edu

Table 2. Planetary and stellar parameters for the rocky exoplanets modelled in this work. Values in parentheses are those used when data is unavailable or rounded values used for a PHOENIX stellar model in the case of Trappist-1 and LHS 3844. Stellar K magnitudes are from 2MASS (Cutri et al. 2003).

Planet	R_p (R_\oplus)	M_p (M_\oplus)	T_{eq} (K)	a (au)	R_s (R_\odot)	T_{eff} (K)	$\log(g_s/\text{cgs})$	[Fe/H]	K mag	Refs
Trappist-1 b	1.086	0.85	400	0.01111	0.117	2559 (2500)	5.2 (5.0)	0.04 (0.0)	10.296	1
GJ 1132 b	1.130	1.66	585	0.0153	0.2105	3270	4.881	-0.12	8.322	2,3,4
LHS 3844 b	1.303	2.25*	807	0.00622	0.189	3036 (3000)	5.06 (5.0)	(0.0)	9.145	5

*Calculated mass assuming an Earth-like composition.

References: 1. Gillon et al. (2017b), 2. Bonfils et al. (2018), 3. Southworth et al. (2017), 4. Berta-Thompson et al. (2015), 5. Vanderspek et al. (2019).

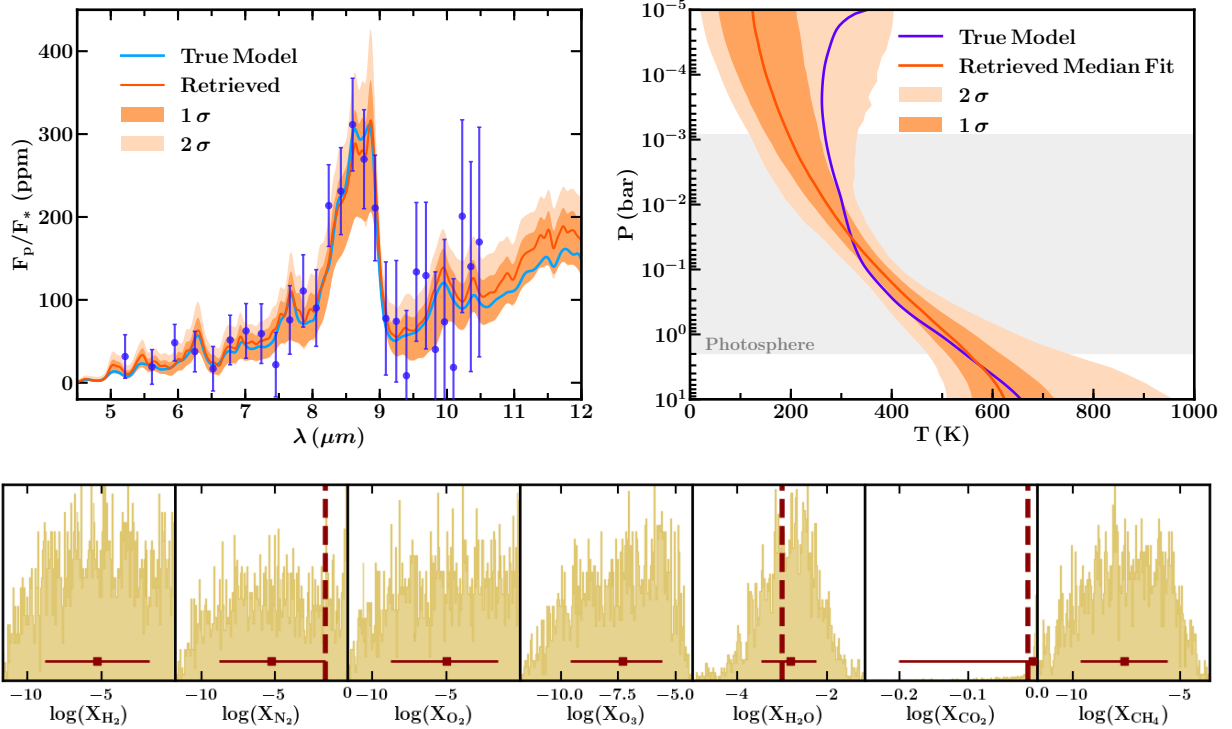


Figure 3. Retrieved emission spectrum, temperature profile and chemical abundances for simulated data of Trappist-1 b, assuming a Venus-like composition. The data are simulated for 30 MIRI LRS eclipses. *Top left:* self-consistently modelled ‘true’ spectrum for Trappist-1 b (blue line) and corresponding simulated MIRI LRS data (purple markers and error bars). The median retrieved spectrum and $1\sigma/2\sigma$ contours are shown by the orange line and dark/light orange shading, respectively. *Top right:* self-consistent ‘true’ temperature profile (purple line) and median retrieved temperature profile and $1\sigma/2\sigma$ contours (orange line and dark/light orange shading, respectively). The shaded grey region shows the range of the 5–20 μm photosphere assuming $R \sim 100$. *Bottom:* Retrieved posteriors for the chemical abundances. ‘True’ input values are shown by vertical dashed lines. Maroon markers and error bars show the median retrieved abundances with 1σ error bars. CO_2 and H_2O are detected at 5.51σ and 4.90σ statistical significance, respectively.

(ii) Recalculate E_p/F_s using a Phoenix spectrum for the star (still assuming a blackbody spectrum for the planet), and use PANDEXO (Batalha et al. 2017) to calculate the uncertainty in the MIRI LRS spectrum.

(iii) Calculate the number of eclipses needed, $E_{S/N=3}$, to achieve a signal-to-noise (S/N) of 3 anywhere in the MIRI LRS range assuming a resolution of $R \sim 10$. We use $E_{S/N=3}$ as a metric for the observability of the target.

By evaluating $E_{S/N=3}$ at a resolution of $R \sim 10$, this metric quantifies the spectroscopic observability of thermal emission from rocky exoplanets and indicates which planets may be amenable to atmospheric characterisation. Since CO_2 and H_2O have broad prominent features in the MIRI LRS spectral range, $R \sim 10$ is a suitable reso-

lution to identify the presence of such species in the atmospheres of rocky exoplanets. For example, we find that the promising rocky exoplanet target GJ 1132 b has $E_{S/N=3}=1.32$, and in section 4 we show that 8 secondary eclipses with MIRI LRS are sufficient to constrain a CO_2 -rich atmosphere. Conversely, fewer eclipses would be required to make photometric detections of the planetary thermal emission, e.g. as discussed by Koll et al. (2019).

Figure 4 shows the observability of the resulting population of rocky exoplanets as a function of their stellar and planetary parameters. As expected, hotter and larger planets are typically more observable than cooler, smaller ones. Furthermore, the number of eclipses required to achieve $S/N=3$ with MIRI LRS increases with host star K magnitude. This suggests that the two main obstacles for observing rocky planet atmospheres in thermal emission are the level

of thermal emission from the planet itself (which affects the measured signal) and the brightness of the host star (which impacts the observational uncertainty). With MIRI LRS, the thermal emission from several hot rocky planets will be observable in fewer than 10 eclipses at $R \sim 10$. However, the characterisation of temperate rocky planet atmospheres will require either more observing time, greater sensitivity than that expected of MIRI, or brighter targets.

We find > 30 rocky exoplanets whose thermal emission will be detectable with $S/N=3$ at $R \sim 10$ in fewer than 10 secondary eclipses (Table C1). We note that, while 55 Cnc e represents an excellent target for thermal emission observations, the brightness of its host star results in partial saturation of the MIRI LRS detector and we therefore exclude it from the present list. Of the rocky exoplanets we consider, the most observable is LHS 3844 b; with an equilibrium temperature of ~ 800 K, it is the only planet in this sample cooler than 1000 K with $E_{S/N=3} < 1$. In the intermediate-temperature regime, GJ 1132 b represents an excellent target and is the only exoplanet cooler than 600 K with $E_{S/N=3} < 4$. In the temperate regime, Trappist-1 b and L 98-59 d both represent ideal targets, having $E_{S/N=3} \sim 10$ and equilibrium temperatures of ~ 400 K.

Our results are consistent with the findings of Koll et al. (2019), who use the emission spectroscopy metric (ESM) of Kempton et al. (2018) to characterise the observability of rocky exoplanets. Concurrent with the trend found in figure 4, they find that the observability of rocky exoplanets in thermal emission typically increases with equilibrium temperature. They also predict that TESS will find ~ 19 exoplanets with radius $< 1.5R_{\oplus}$ and an ESM greater than that of GJ 1132 b (which is considered to be an optimal rocky exoplanet candidate for atmospheric characterisation, e.g. Morley et al. 2017). By considering known exoplanets with masses $< 10M_{\oplus}$ and radii $< 2R_{\oplus}$, we find in this work that at least 14 known exoplanets are more observable than GJ 1132 b according to our observability metric. These include the 3 known planets identified by Koll et al. (2019) as having an ESM greater than that of GJ 1132 b, i.e. HD 213885 b, LHS 3844 b and 55 Cnc e.

In Section 4, we perform a more detailed analysis of the three promising targets Trappist-1 b, GJ 1132 b, and LHS 3844 b. These planets each represent ideal targets for their respective equilibrium temperatures, which span the temperate to hot regimes (~ 400 – 800 K). We note that the estimated number of eclipses calculated here for a S/N of 3 is not exact due to the assumption of blackbody spectra, and characterises the ease with which thermal emission from the planet can be observed rather than the number of eclipses required to make chemical detections. However, this analysis does provide a simple metric to assess ideal targets for characterising rocky exoplanet atmospheres, and can guide more detailed evaluations such as those in Section 4. Indeed, this simple analysis shows that a large number of known rocky exoplanets are suitable targets for atmospheric characterisation in thermal emission with JWST.

4 RESULTS

We investigate the observability of key molecular species in rocky exoplanet atmospheres using three promising candidates as case studies: Trappist-1 b, GJ 1132 b and LHS 3844 b, which span the ~ 400 – 800 K equilibrium temperature range (Berta-Thompson et al. 2015; Gillon et al. 2016; Vanderspek et al. 2019). In particular, we consider three different atmospheric compositions including a cloud-free Venus-like (CO_2 -rich) atmosphere, a 50% CO_2 /50% H_2O atmosphere and a 100% H_2O atmosphere (see Section 2.2). For each planet and atmospheric composition, we first model the thermal emis-

sion spectrum and simulate JWST MIRI data, as described in Section 2.2. The model spectra for each case study are shown in Figures 5 and 6, including simulated MIRI data. We then perform atmospheric retrievals on this simulated data and assess the detection significances of the key molecular species in each case, as detailed in Section 2.1. We assume full day-night energy redistribution for all our models as this provides a conservative estimate of the observations required to make chemical detections; less efficient heat redistribution would result in a hotter day-side and a deeper secondary eclipse. However, we note that LHS 3844 b's observed phase curve has a strong day-night contrast (Kreidberg et al. 2019) which indicates inefficient day-night heat transport and a hotter day-side than assumed here. The observability estimates we provide here are therefore conservative.

For each of the atmospheres investigated here, we take a hierarchical approach by considering four key science cases to be addressed, in order of increasing scientific complexity:

- (i) **Comparison to a bare rock with no energy redistribution:** A solid, bare rocky surface is expected to be significantly hotter than an atmosphere with energy redistribution, and may be observationally distinguished from an atmosphere with efficient energy redistribution (Koll et al. 2019). We consider whether the simulated data are enough to rule out this hot bare rock scenario, indicating energy redistribution e.g. due to an atmosphere or magma ocean.
- (ii) **Presence of spectral features:** Can the observations statistically rule out a blackbody spectrum? If so, the presence of absorption or emission features confirms the presence of an atmosphere and an atmospheric temperature gradient.
- (iii) **Detection of CO_2 :** CO_2 has a sharp spectral feature at $\sim 9 \mu\text{m}$ (Figure 2) which can be observed in MIRI LRS spectra. CO_2 is therefore one of the easiest molecules to detect in this spectral range if it is sufficiently abundant in the atmosphere.
- (iv) **Detection of H_2O :** With sufficient spectral precision, H_2O can be detected and its atmospheric abundance can be measured.

In what follows, we investigate these four science cases for each planet and atmospheric composition. The retrieved thermal emission spectra, temperature profiles and posterior probability distributions for the chemical abundances are shown for each case investigated in Figures 6, 7 and 8, respectively.

4.1 Case Study: LHS 3844 b

LHS 3844 b is a highly-irradiated rocky planet orbiting a nearby M-dwarf, with a dayside temperature of ~ 1000 K (Kreidberg et al. 2019; Vanderspek et al. 2019). Recent phase curve observations of the planet have revealed a strong day-night temperature contrast and no hotspot shift, ruling out the possibility of an atmosphere with pressure $\gtrsim 10$ bar (Kreidberg et al. 2019). Recent observations of LHS 3844 b with transmission spectroscopy are further inconsistent with a clear, H_2 -rich atmosphere of pressure $\gtrsim 0.1$ bar and suggest either a high- μ atmosphere, a H_2 -rich atmosphere with high-altitude clouds (cloud-top pressures < 0.1 bar) or no atmosphere at all (Diamond-Lowe et al. 2020).

Thermal emission spectroscopy will be required to assess the presence of an atmosphere on LHS 3844 b. Even in the case of a high- μ atmosphere, which can be prohibitive for transmission spectroscopy, the thermal emission spectrum can be sensitive to molecular absorption/emission features. Here, we assess whether observations with JWST/MIRI could constrain the presence of an atmosphere on LHS 3844 b assuming a cloud-free Venus-like, 50% CO_2 /50% H_2O and 100% H_2O composition. For this case study we consider three observing strategies: (i) a shorter observing time strategy with 8

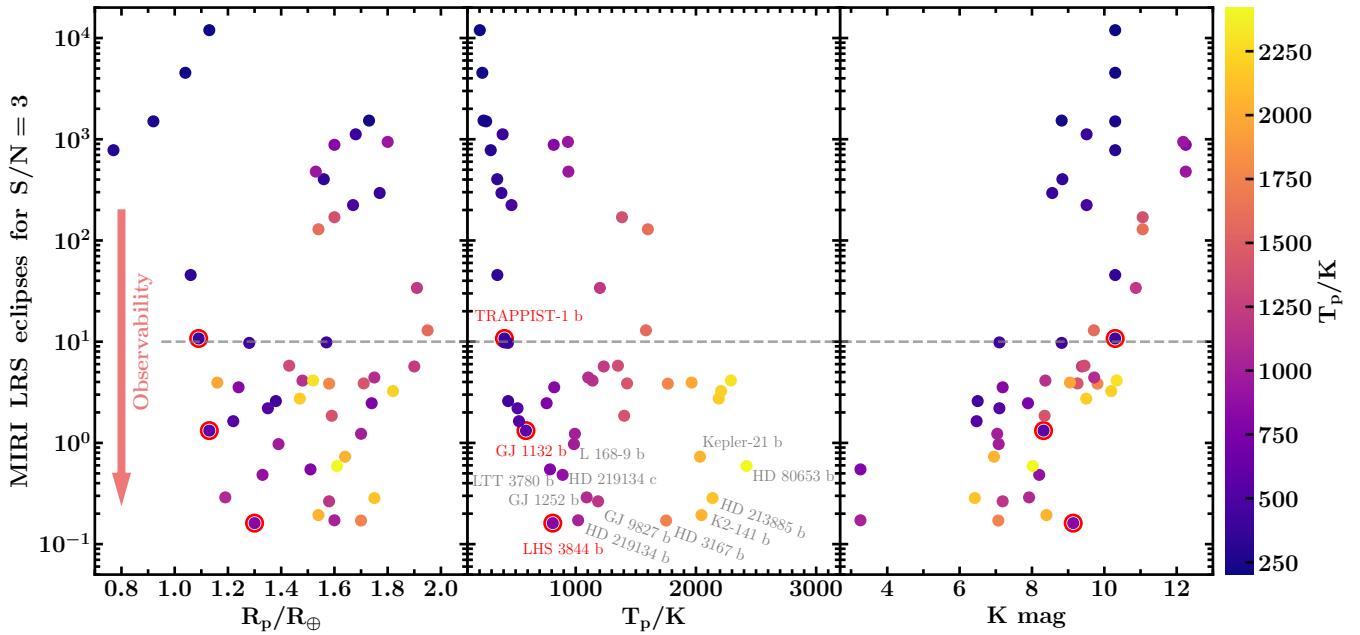


Figure 4. Observability of known rocky planets in thermal emission as a function of planet radius (R_p , left panel), equilibrium temperature (T_p , centre panel) and K magnitude of the host star (right panel). Observability is defined as the number of secondary eclipses with MIRI LRS required to detect the thermal emission of the planet, F_p/F_s , at $S/N=3$ assuming a resolution of $R\sim 10$. Note that non-integer numbers of eclipses would need to be rounded up as partial transits would not contribute as much to the S/N. The targets shown here are chosen such that $F_p/F_s > 10$ ppm in the MIRI LRS spectral range (i.e. 5–12 μm). In each panel, the markers for each planet are coloured according to planet equilibrium temperature (see colourbar). The case studies LHS 3844 b, GJ 1132 b and Trappist-1 b are circled in red in each panel, for reference. The horizontal dashed line denotes 10 eclipses required with MIRI LRS for a $S/N=3$. The planets below this line represent optimal targets for atmospheric characterisation in thermal emission with JWST MIRI, and their properties are listed in Table C1. Note that 55 Cnc e is not shown here as it would saturate part of the MIRI LRS detector.

MIRI LRS eclipses, (ii) a longer strategy with 20 MIRI LRS eclipses and (iii) a strategy with 20 MIRI LRS eclipses plus 4 eclipses with the MIRI imager F1500W photometric band. The simulated spectra and data are shown in the top panel of Figure 5 and the top three rows of Figure 6.

From Figure 5, it is clear that the uncertainties on the data using 20 MIRI LRS eclipses and/or the photometry allow the Venus-like, 50% CO_2 /50% H_2O and 100% H_2O compositions to be distinguished, especially at wavelengths $\gtrsim 9 \mu\text{m}$. For the longer observing strategies, the data also significantly deviate from a blackbody spectrum for all three compositions considered; for example, the sharp CO_2 feature at $\sim 9 \mu\text{m}$ can easily be distinguished for the Venus-like and 50% CO_2 /50% H_2O models. For the shortest observing strategy of 8 MIRI LRS eclipses, the Venus-like and 100% H_2O cases can also be significantly distinguished from a blackbody spectrum. A bare-rock surface (assuming no energy redistribution, grey spectrum in the top panel of Figure 5) is also evidently rejected by the simulated data for all compositions and observing strategies.

For each atmospheric composition considered, we perform an atmospheric retrieval on the simulated MIRI data described above. The retrieved spectra, temperature profiles and posterior probability distributions for the chemical abundances are shown in the top three rows of Figures 6, 7 and 8, respectively, for each case. The ‘true’ input spectra are retrieved within 2σ for all three atmospheric compositions, within the spectral range of the data. In all cases, the abundances of H_2O and CO_2 are accurately retrieved within 2σ , though in the case of only 8 MIRI LRS eclipses for the 50% H_2O /50% CO_2 and 100% H_2O compositions, these are not detected with statistical

significance (Table 3). Furthermore, the temperature profile of each atmosphere is accurately retrieved to within $\sim 2\sigma$ in the photosphere. Outside the photosphere, the observed spectrum does not contain information about the temperature profile and it is therefore expected that the retrieved temperature profile may deviate in this range.

We further evaluate the confidence with which the data reject a blackbody spectrum and the confidence with which CO_2 and H_2O are detected, as described above and in Section 2.1.3. With only 8 MIRI LRS eclipses, we find that CO_2 and H_2O can confidently be detected in the Venus-like case, with detection significances of 5.55σ and 4.07σ , respectively (Table 3). Furthermore, while the 50% H_2O /50% CO_2 and 100% H_2O cases are more challenging to characterise with only 8 eclipses, a blackbody spectrum can be rejected at $\lesssim 3\sigma$ for the 100% H_2O composition. 8 MIRI LRS eclipses are therefore sufficient to characterise a cloud-free Venus-like composition on LHS 3844 b, or to tentatively detect atmospheric absorption (i.e. reject a blackbody spectrum) in the case of a 100% H_2O atmosphere.

For the two longer observing time strategies, i.e. with at least 20 MIRI LRS eclipses, stronger constraints can be obtained for all three compositions considered (Table 3). For both the Venus-like and 50% H_2O /50% CO_2 cases, we find that CO_2 and H_2O can be detected with $\gtrsim 4\sigma$ significance. The 100% H_2O composition remains more challenging to characterise, but these longer observing time strategies do allow a blackbody spectrum to be rejected at a higher confidence of $> 4\sigma$, compared to the 8 eclipse strategy. 20 MIRI LRS eclipses are therefore sufficient to characterise cloud-free, CO_2 -rich compositions for LHS 3844 b, or to confidently detect atmospheric

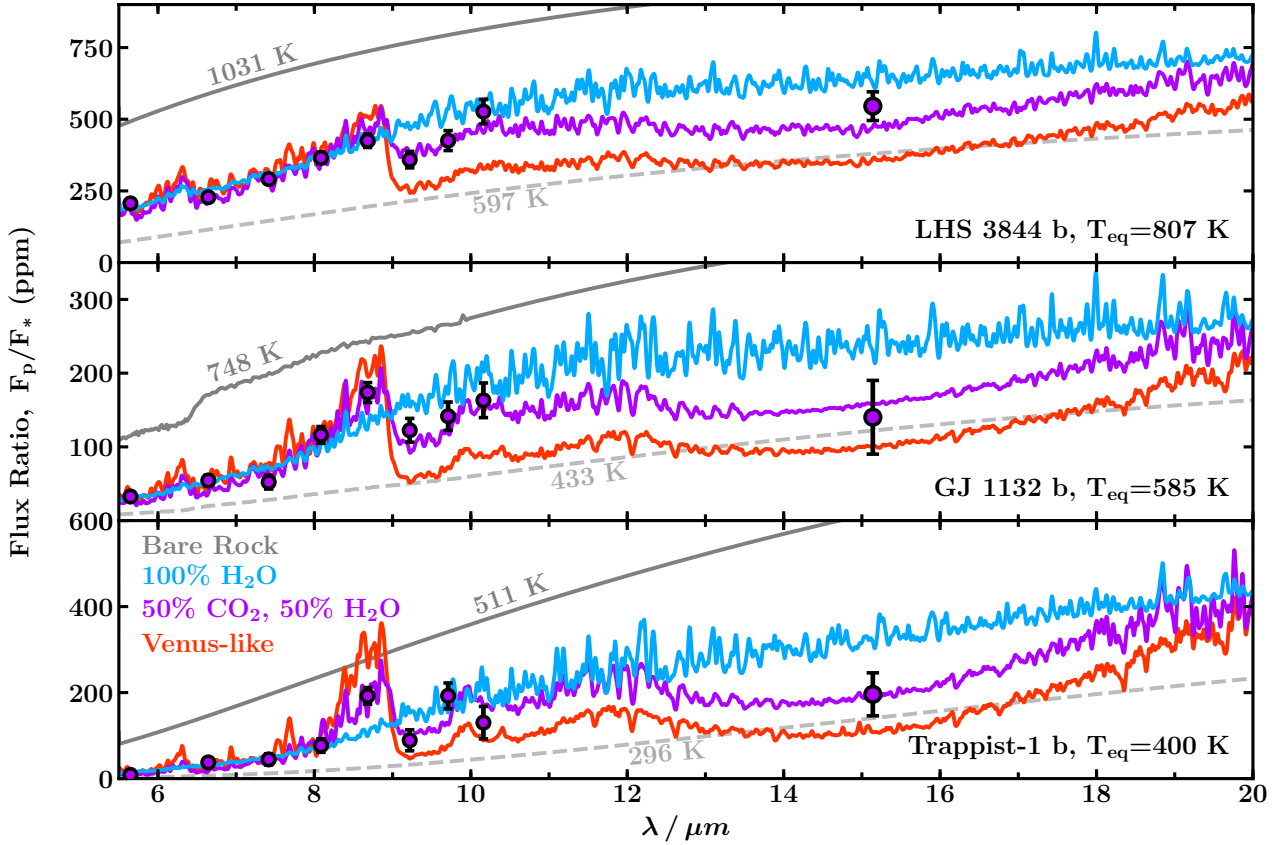


Figure 5. Thermal emission spectra for LHS 3844 b, GJ 1132 b and Trappist-1 b assuming Venus-like (red lines), 50% CO₂/50% H₂O (purple lines) or 100% H₂O (blue lines) compositions. Blackbody spectra corresponding to the temperature expected for a bare rock with no energy redistribution are also shown by solid grey lines. Dashed grey lines show blackbody spectra corresponding to the equilibrium temperature expected for a Venus-like Bond albedo of 0.7. Data points and error bars show simulated MIRI LRS data and photometric data in the F1500W bandpass. The error bars assume 20 MIRI LRS eclipses for LHS 3844 b and GJ 1132 b, and 80 eclipses for Trappist-1 b. Note that the LRS data are binned for clarity. The photometric points have error bars of 50 ppm for all three targets, corresponding to ~ 4 eclipses each.

absorption in the case of a 100% H₂O atmosphere. We note that the addition of the four photometric eclipses does not significantly improve the retrieved constraints beyond what is achieved with 20 MIRI LRS eclipses alone. Furthermore, for all three observing strategies considered here, the abundances of CO₂ and H₂O (when detected) can be measured to within $\lesssim 0.5$ dex across the compositions we have considered here, i.e. comparable to the precision achieved for chemical abundances in hot Jupiters to date (e.g. Sheppard et al. 2017; Welbanks et al. 2019).

4.2 Case Study: GJ 1132 b

GJ 1132 b is a small rocky exoplanet with an equilibrium temperature of ~ 600 K (Berta-Thompson et al. 2015). Thanks to its nearby host star and large planet-star size contrast, this planet is an ideal candidate for thermal emission spectroscopy of warm rocky planets (Morley et al. 2017). To date, atmospheric observations of GJ 1132 b using transmission spectroscopy have revealed a relatively flat spectrum, consistent with a high- μ atmosphere (Southworth et al. 2017; Diamond-Lowe et al. 2018). Thermal emission spectroscopy will be needed to confirm the presence of this atmosphere and to establish its chemical composition. Here, we consider the JWST/MIRI obser-

vations needed to constrain the presence and chemical composition of an atmosphere on GJ 1132 b assuming a cloud-free Venus-like (CO₂-rich), 50% CO₂/50% H₂O or 100% H₂O composition.

In order to characterise the observability of GJ 1132 b, we investigate the same three observing strategies used above for LHS 3844 b, i.e.: (i) 8 eclipses with MIRI LRS, (ii) 20 eclipses with MIRI LRS, (iii) 20 eclipses with MIRI LRS plus 4 eclipses with the F1500W photometric band. The simulated spectra and data for these cases are shown in Figure 5 and the middle three rows of Figure 6, respectively. For all three observing strategies, the data are clearly distinguishable from the solid bare-rock scenario with no energy redistribution (grey spectrum in Figure 5). For the Venus-like composition, the observational uncertainties for each strategy are further sufficient to distinguish the strong CO₂ feature at $\sim 9 \mu\text{m}$. The retrieved spectra, temperature profiles and posterior distributions for each composition and observing strategy are shown in the middle three rows of Figures 6, 7 and 8, respectively.

With the assumption of 8 MIRI LRS eclipses, we find that the Venus-like composition is confidently constrained, with 4.7σ and 4.4σ detections of CO₂ and H₂O, respectively (Table 3). CO₂ and H₂O are not confidently detected for the 50% CO₂/50% H₂O and 100% H₂O compositions using this strategy, but in the 100% H₂O

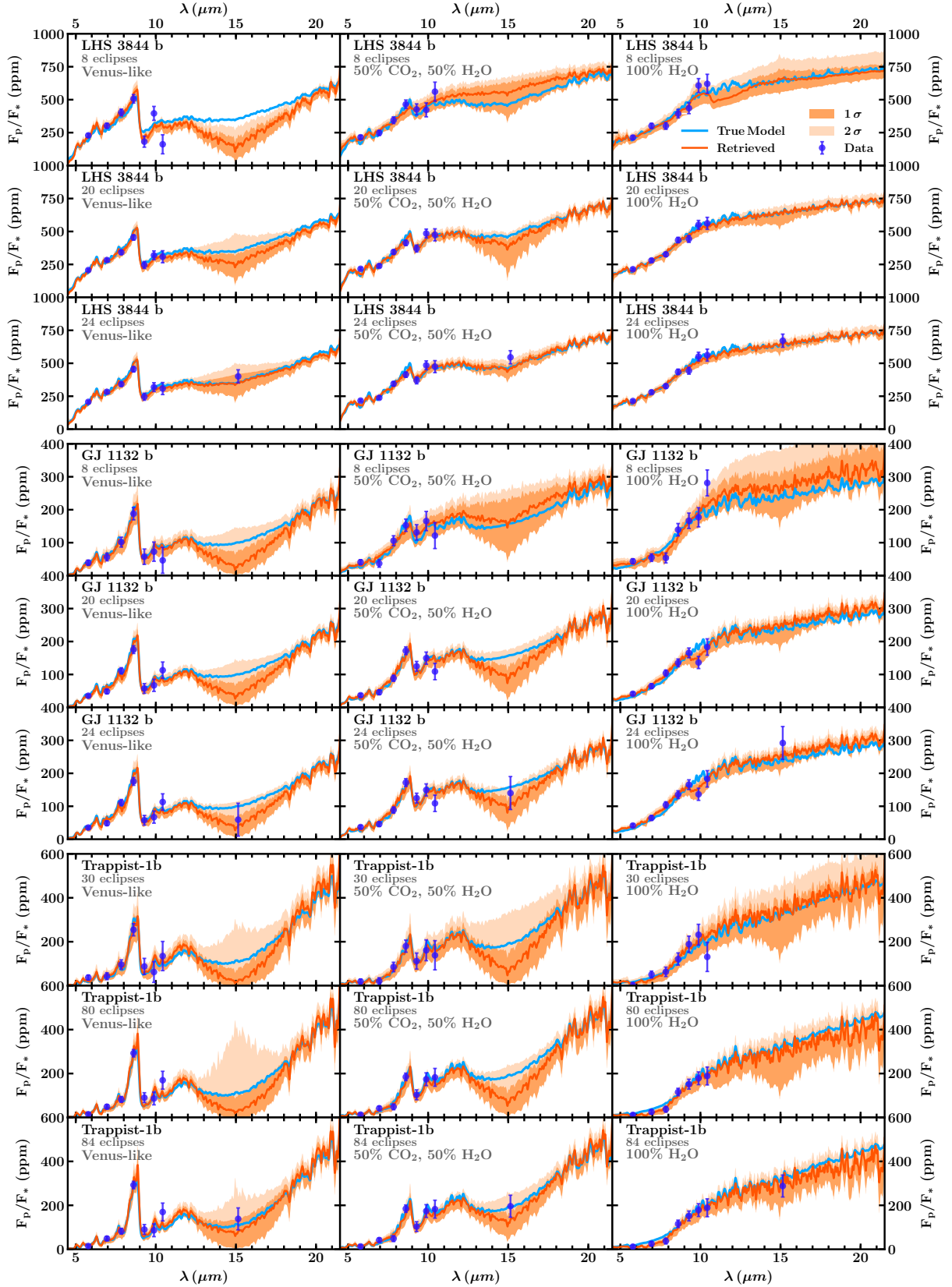


Figure 6. Retrieved thermal emission spectra for LHS 3844 b (top three rows), GJ 1132 b (middle three rows) and Trappist-1 b (bottom three rows) for the simulated data described in section 4 assuming a Venus-like, 50% CO₂/50% H₂O or 100% H₂O composition (left, centre and right columns, respectively). Dark orange lines show the median retrieved spectrum, while dark and light orange shaded regions show 1 σ and 2 σ confidence intervals. Purple points and error bars show simulated MIRI LRS and photometric data, as described in Section 4. The light blue line shows the ‘true’ input spectrum.

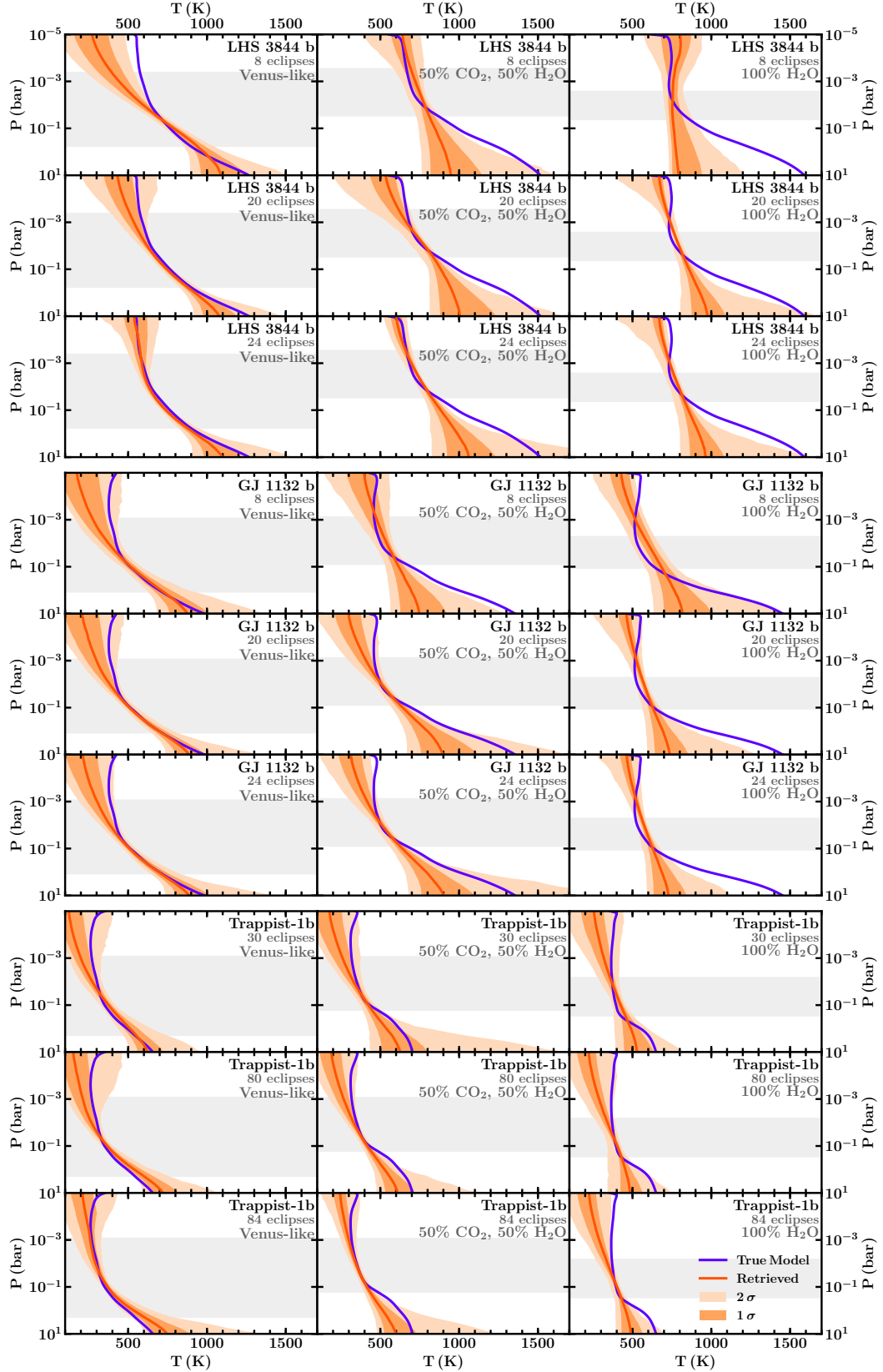


Figure 7. Retrieved temperature profiles for LHS 3844 b (top three rows), GJ 1132 b (middle three rows) and Trappist-1 b (bottom three rows) for the simulated data described in section 4 assuming a Venus-like, 50% CO₂/50% H₂O or 100% H₂O composition (left, centre and right columns, respectively). Dark orange lines show the median retrieved temperature profile, while dark and light orange shaded regions show 1 σ and 2 σ confidence intervals. Purple lines show the ‘true’ input temperature profile. Shaded grey regions show the range of the 5–20 μ m photosphere assuming $R \sim 100$.

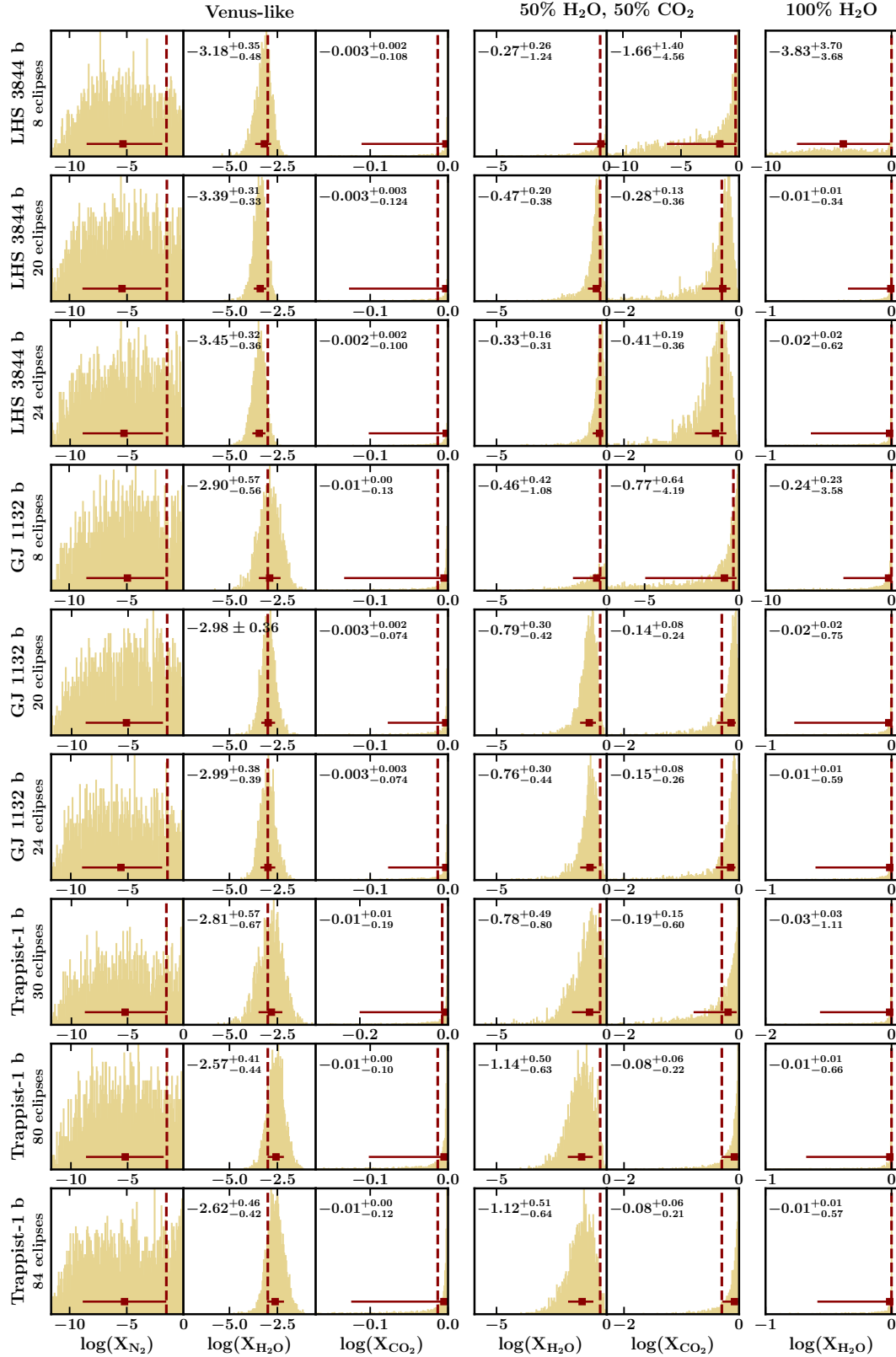


Figure 8. Posterior probability distributions for the species present in each simulated data model, i.e. N_2 , H_2O and CO_2 for the Venus-like composition (three left columns), H_2O and CO_2 for the 50% CO_2 /50% H_2O composition (4th and 5th columns) and H_2O for the 100% H_2O composition (right column). Note that the retrieval model includes all the species discussed in Section 2.1.2, but species not present in the simulated data (i.e. those not shown here) are not constrained. Posteriors are shown for the case studies LHS 3844 b (top three rows), GJ 1132 b (middle three rows) and Trappist-1 b (bottom three rows) for the simulated data described in section 4. ‘True’ input values are shown by vertical dashed lines. Median retrieved abundances and 1σ uncertainties are given for each CO_2 and H_2O posterior distribution, and are shown by maroon markers and error bars for all posteriors. Note that the abundance of N_2 is unconstrained in the Venus-like case due to its lack of spectral features in the wavelength range considered. The H_2O posteriors for the 100% H_2O composition are typically strongly peaked at 100%.

case a blackbody spectrum is nevertheless rejected at $> 4\sigma$. The spectra are retrieved to within 2σ in the spectral range of the data, while the temperature profiles are also retrieved to within 2σ in the photosphere. Furthermore, the abundances of CO_2 and H_2O are accurately retrieved to within 2σ . For the Venus-like case, the abundances of CO_2 and H_2O are constrained within < 0.6 dex. This relatively short observing time strategy would therefore be suitable for determining whether GJ 1132 b is a cloud-free exo-Venus.

For the longer observing time strategies, i.e. using 20 MIRI LRS eclipses, we find that $\geq 3\sigma$ detections of both CO_2 and H_2O can be made across all three atmospheric compositions (Table 3). In particular, confident, $\sim 4\text{--}8\sigma$ detections of these species can be made in the Venus-like and 50% CO_2 /50% H_2O cases. The 100% H_2O case is slightly more challenging to characterise, allowing $\sim 3\sigma$ detections of H_2O with these observing strategies. We note, however, that the addition of four eclipses with the F1500W filter on top of the 20 MIRI LRS eclipses does not significantly improve the atmospheric constraints which are made. The spectra and temperature profiles are all retrieved to within 2σ , while the abundances of CO_2 and H_2O are accurately retrieved within 1σ uncertainties of ≤ 0.75 dex. We therefore conclude that these longer observing time strategies would be able to characterise the atmosphere of GJ 1132 b across a range of CO_2 - and H_2O -rich compositions, including determining the abundances of these two species. Given the importance of CO_2 and H_2O in geochemical processes, such constraints would be invaluable in determining the possible atmospheric origins of GJ 1132 b.

4.3 Case Study: Trappist-1 b

The Trappist-1 system (Gillon et al. 2016, 2017b) is currently the most promising system of terrestrial-like exoplanets for atmospheric characterisation (Turbet et al. 2020). Thanks to the host star's small radius ($0.117 R_\odot$) and low effective temperature (2559 K), the secondary eclipse depths of the Trappist-1 planets are favourable despite the small planetary sizes and low planetary temperatures. In particular, Trappist-1 b is the warmest planet in this system, with an equilibrium temperature of 400 K, and represents an excellent candidate for atmospheric characterisation of a temperate exoplanet in thermal emission. Meanwhile, transmission spectroscopy observations have already begun to place constraints on the atmosphere of Trappist-1 b. de Wit et al. (2016) rule out a clear, H_2 -rich atmosphere at $> 10\sigma$ and note that while a H_2 -rich atmosphere with high-altitude clouds/hazes is allowed by the data, this is an unlikely scenario given the relatively low irradiation level of Trappist-1 b. Conversely, Bourrier et al. (2017) find a marginal decrease in the Lyman- α flux of Trappist-1 during the transits of planets b and c, which may indicate the presence of extended hydrogen exospheres. However, this effect could also be caused by stellar activity. A secondary atmosphere on Trappist-1b therefore remains a promising possibility, and we investigate the observability of a Venus-like, 50% CO_2 /50% H_2O and 100% H_2O atmosphere.

Compared to LHS 3844 b and GJ 1132 b, Trappist-1 b's relatively small planetary radius and cooler temperature results in a lower S/N and the need for longer observation times. Here, we consider three observation strategies: (i) 30 eclipses with MIRI LRS, (ii) 80 eclipses with MIRI LRS, (iii) 80 eclipses with MIRI LRS plus 4 eclipses with the F1500W photometric band. The bottom panel of Figure 5 shows the simulated spectra for Trappist-1 b across the CO_2 -rich to H_2O -rich compositions considered here, while the bottom three rows of Figure 6 show the simulated data and retrieved spectra. For all three observational strategies, the data are clearly distinguishable from the bare-rock scenario with no energy redistribution. Furthermore, for

the Venus-like composition, the sharp CO_2 feature at $\sim 9 \mu\text{m}$ can be distinguished by eye, consistent with the confident detections of CO_2 in these retrievals.

Assuming 30 MIRI LRS eclipses, we find that CO_2 and H_2O are detected in both the Venus-like and 50% CO_2 /50% H_2O cases (Table 3). The Venus-like composition is most confidently constrained, with 5.5σ and 4.9σ detections of CO_2 and H_2O , respectively, while the 50% CO_2 /50% H_2O composition leads to $\sim 3\sigma$ detections of these species. However, in the 100% H_2O case the simulated data are consistent with a blackbody and spectral features are not detected with statistical significance. Nevertheless, for all three compositions the retrieval framework fits the true spectrum and photospheric P - T profile within 2σ uncertainties (Figure 7). This 30-eclipse strategy would therefore be ideal to characterise (or rule out) clear, CO_2 -dominated atmospheric compositions on Trappist-1 b.

Using a longer observing time of 80–84 eclipses, we find that the Venus-like and 50% CO_2 /50% H_2O compositions are readily characterised, allowing $\sim 4\text{--}10\sigma$ detections of CO_2 and H_2O (Table 3). The 100% H_2O composition is more challenging to characterise, though a blackbody spectrum is nevertheless rejected by the data at $\sim 4\sigma$ with both of these observing strategies. For all three compositions, both the spectra and temperature profiles are retrieved within 2σ , while the abundances of CO_2 and H_2O are retrieved to within the 2σ uncertainties. We note that these results are very similar for both the observing strategies with and without the photometry, suggesting that the MIRI LRS data is driving these detections. 80 eclipses using MIRI LRS are therefore sufficient to confidently characterise cloud-free CO_2 -rich compositions for Trappist-1 b, and to detect the presence of atmospheric absorption in the case of a water-rich composition. Furthermore, across all of the observing strategies discussed here, the abundances of CO_2 and H_2O are constrained to within $1\text{--}\sigma$ uncertainties of < 0.7 dex, where these species are detected.

5 DISCUSSION

In section 4, we have shown that rocky exoplanet atmospheres across a wide range of temperatures ($\sim 400\text{--}800$ K) can be characterised in thermal emission with JWST/MIRI, including confident detections of atmospheric absorption by CO_2 and H_2O . Here, we begin by discussing the calculation of detection significances and key subtleties which can arise. Having focused on cloud- and haze-free atmospheric compositions in previous sections, we also discuss the impact which clouds and hazes may have on the characterisation of rocky exoplanet atmospheres in Section 5.2. In sections 5.3 and 5.4, we also discuss 3D effects and stitching together multi-mode observations.

5.1 Detection Significances

When considering detection significances, it is useful to understand the role of model complexity in determining the Bayesian evidence. As described in Section 2.1.3, the confidence of a molecular detection can be assessed by comparing the Bayesian evidences of two retrievals including/excluding the molecule(s) in question. Similarly, the confidence with which a blackbody spectrum can be rejected can be assessed by comparing the Bayesian evidences of retrievals with a full atmospheric model vs. only a single temperature (i.e. a blackbody model). However, these Bayesian evidences encapsulate not only the fit to the spectrum but also the complexity of the model. For example, if a 10-parameter model results in the same goodness of fit as a 5-parameter model, the 5-parameter model will have a higher Bayesian evidence as it has a lower model complexity.

Table 3. Detection significances for CO₂ and H₂O given different atmospheric compositions and observing strategies for LHS 3844 b, GJ 1132 b and Trappist-1 b (see Section 4). The confidence level at which the data eliminates a blackbody spectrum is also shown for each case (columns labelled ‘non-BB’). The number of eclipses with MIRI LRS and MIRI photometry assumed for each case are shown in italics. Confidence levels below 2σ are not shown.

Planet	Venus			50% H ₂ O/50% CO ₂			100% H ₂ O	
	CO ₂	H ₂ O	non-BB	CO ₂	H ₂ O	non-BB	H ₂ O	non-BB
LHS 3844 b								
<i>8 LRS</i>	5.55	4.07	8.37	–	2.52	2.28	–	2.93
<i>20 LRS</i>	7.06	5.32	10.59	3.87	5.02	4.86	2.74	4.20
<i>20 LRS, 4 F1500W</i>	6.95	5.20	11.00	3.61	4.72	4.45	2.82	4.50
GJ 1132 b								
<i>8 LRS</i>	4.70	4.42	5.69	–	2.68	2.31	–	4.38
<i>20 LRS</i>	7.62	6.91	8.75	4.35	4.53	5.03	3.18	3.20
<i>20 LRS, 4 F1500W</i>	8.05	6.90	9.20	4.76	5.05	5.33	2.96	3.20
Trappist-1 b								
<i>30 LRS</i>	5.51	4.90	5.82	2.89	3.40	3.02	2.31	2.47
<i>80 LRS</i>	9.09	9.60	11.06	4.40	4.68	4.75	2.50	4.08
<i>80 LRS, 4 F1500W</i>	9.79	9.57	11.73	4.86	4.70	4.98	2.65	3.90

When calculating the detection significance of a single molecule, the models compared only have a difference of one parameter (i.e. the models are identical apart from the presence of one molecule), and so the detection significance calculated from this comparison is a fairly good measure of ‘goodness of fit’ as the model complexities are comparable. However, when the ‘full model’ is compared to a blackbody model, there is a significant difference in model complexity (i.e. 13 parameters for the full model vs 1 parameter for the blackbody). This means that the full model is penalised for its complexity relative to the blackbody model, and the blackbody spectrum may be rejected at a lower significance than expected. That is, the poor fit from a blackbody model may be compensated for by the simplicity of the model.

An alternative way to assess how confidently a blackbody model can be rejected is to compare this model to a ‘core parameters’ model. This ‘core parameters’ model is based on the full atmospheric model, but includes only the species for which there is evidence in the data. For example, if H₂O and CO₂ are detected in the data (using the full model) but no other species are detected, the ‘core parameters’ model would include only H₂O and CO₂ (as well as the usual temperature profile parameterisation). This effectively strips down the full model to the components which are necessary to fit the data, without including unnecessary parameters. Thus, when compared to the blackbody model, the ‘core parameters’ model is not penalised by unnecessary parameters, and instead the difference in model complexity is more representative of the complexity required to fit the data. For example, in the Venus-like case for Trappist-1 b with 30 MIRI LRS eclipses, comparing the blackbody model to the ‘core parameters’ model results in a 6.09σ rejection of the blackbody, whereas a comparison to the full model results in a 5.82σ rejection. Note that all detection significances shown in Table 3 use a comparison with the full model.

Ultimately, it is important to understand how the models used can affect the confidence with which a blackbody spectrum can be rejected. In cases with very strong molecular detections (e.g. the LHS 3844 b case study shown here, first row of Table 3), a blackbody can be rejected with high confidence even when compared to the full model. In more marginal cases, however, it may be necessary to consider how model complexity affects this metric. We further note that confident molecular detections provide a robust way to reject

a featureless spectrum as the model comparisons involved in this calculation are not subject to large differences in model complexity.

5.2 Impact of Clouds and Hazes

Clouds and hazes can have significant effects on the temperature profiles and thermal emission spectra of low-mass exoplanets (e.g. Morley et al. 2015; Piette & Madhusudhan 2020a). So far in this work we have considered clear atmospheres, and we now discuss how clouds and hazes may affect the atmospheric characterisation of rocky exoplanets. While optical scattering from clouds and hazes is not directly visible in infrared observations, it has the effect of cooling the atmosphere and results in a more isothermal temperature profile. This can lead to a smaller planetary flux and muted spectral features, as demonstrated by Piette & Madhusudhan (2020a) for mini-Neptunes. However, while cloudy atmospheres may provide challenges for chemical detections, secondary eclipse observations can still constrain atmospheric properties above the cloud deck, including the photospheric temperature (Piette & Madhusudhan 2020a).

For the case studies LHS 3844 b, GJ 1132 b and Trappist-1 b, we consider the observability of the atmosphere given strong optical scattering from clouds and hazes. Figure 5 shows blackbody spectra for each of these planets at an equilibrium temperature which assumes a Venus-like Bond albedo of 0.7 and full day-night energy redistribution (light grey dashed lines). For LHS 3844 b, this spectrum would be detectable at $>3\sigma$ with MIRI LRS in 8 eclipses (e.g. for the resolution shown in Figure 6) or in the F1500W band in four eclipses. While spectral features may not necessarily be distinguishable due to the cloud opacity, the photospheric temperature could be constrained from such a detection. GJ 1132 b has a lower S/N ratio but would be detectable at $>3\sigma$ with 20 MIRI LRS eclipses (e.g. at the resolution shown in Figure 5). Trappist-1 b would be more challenging to detect with MIRI LRS, but four eclipses in the F1500W band could be sufficient to detect the atmosphere and measure its photospheric temperature.

We therefore conclude that the atmospheres of LHS 3844 b, GJ 1132 b and Trappist-1 b would be observable with MIRI even in the case of an extreme, Venus-like Bond albedo. Furthermore, a measurement of the photospheric temperature in this case would

allow a joint constraint on the Bond albedo and day-night energy redistribution of the planet, which are degenerate in determining the dayside equilibrium temperature. For example, a photospheric temperature of ~ 430 K for GJ 1132 b would suggest a high Bond albedo of $\sim 0.7/0.85$, assuming efficient day-night energy redistribution/no day-night energy redistribution, respectively. In between the clear and Venus-like albedo cases, more moderate clouds and hazes may result in muted spectral features that can still be characterised using spectral retrieval analysis. JWST/MIRI observations of such rocky exoplanets will therefore place important constraints on their atmospheric properties, regardless of the presence of clouds and hazes.

5.3 3-D effects

3-dimensional effects are known to impact thermal emission observations of exoplanet atmospheres, especially those which are tidally-locked (e.g. Showman et al. 2009; Knutson et al. 2007; Demory et al. 2016; Kreidberg et al. 2019). While efficient energy redistribution can act to homogenise the dayside atmosphere, dayside temperature and/or compositional inhomogeneities can have observable effects on the secondary eclipse spectrum of the atmosphere (e.g. Feng et al. 2020; Taylor et al. 2020; Cubillos et al. 2021). For rocky exoplanets, a higher equilibrium temperature and/or lower surface pressure typically leads to less efficient day-night energy redistribution (Koll & Abbot 2016), with redistribution becoming efficient at surface pressures of $O(1)$ bar (Koll 2019). Therefore, the degree of longitudinal variation on the daysides of rocky exoplanets may vary considerably between different targets, depending on their atmospheric properties. In cases of more extreme inhomogeneity, it has been demonstrated for hot Jupiters that 1-D retrievals can result in biased results, depending on the signal-to-noise ratio of the data (e.g. Feng et al. 2020; Taylor et al. 2020; Cubillos et al. 2021). It is therefore useful to place the results of 1-D atmospheric secondary eclipse retrievals into context, e.g. using multi-dimensional retrievals (e.g. Feng et al. 2016, 2020; Taylor et al. 2020) or with complementary phase curve observations. Nevertheless, 1-D retrievals can provide a valuable first glimpse into the dayside atmospheres of rocky exoplanets, especially considering the data quality expected for rocky exoplanets with JWST.

Ultimately, phase curve observations are required to deconstruct the longitudinal structure of an exoplanet atmosphere. Several methods exist to extract longitudinal information from such observations (e.g. Feng et al. 2016, 2020; Irwin et al. 2020; Cubillos et al. 2021). In particular, Cubillos et al. (2021) present a new approach in which a 1-D retrieval is applied to each ‘slice’ in a longitudinally-deconstructed phase curve, applying it to the phase curve of the hot Jupiter WASP-43 b. Such an approach could be used to extend HyDRo to interpret the phase curves of rocky exoplanets.

5.4 Stitching Multi-Mode Observations

For each of the more time-intensive MIRI LRS observing strategies considered in Section 4, we have investigated the impact of using MIRI LRS observations both with and without additional photometric observations with the F1500W filter. As discussed in Section 4, this additional photometric data does not significantly improve the chemical detections which can be made with MIRI LRS alone. Additionally, it would be important to consider possible systematic offsets between different instrument modes, which are as yet uncharacterised for JWST and may lead to spurious detections (see e.g. Barstow et al. 2015). Future characterisation of the MIRI instrument may allow for the stitching of MIRI LRS and MIRI photometry data, for example

by calibrating these modes with multiple measurements of the same source at high S/N. Meanwhile, the cases explored here argue that a MIRI LRS-only approach is able to characterise rocky exoplanet atmospheres with CO_2 -rich to H_2O -rich compositions, independent of the photometry. We additionally note that, while effects due to stellar activity may hinder the stitching of transmission spectra, this is not the case for secondary eclipse spectra (e.g. Barstow et al. 2015).

6 CONCLUSIONS

In this work, we develop the first retrieval framework for thermal emission spectra of rocky exoplanets, HyDRo. This framework is able to retrieve the chemical composition of the atmosphere without assuming a particular background species, using the centered-log-ratio chemical abundance parameterisation of Benneke & Seager (2012). The method is therefore ideally suited for determining the chemistry of secondary atmospheres, with implications for the study of exo-geology. The retrieval framework is further able to constrain the atmospheric temperature profile, providing important information about the thermal properties and potential surface conditions of the planet.

In order to test the retrieval framework, we generate self-consistent atmospheric models and simulated JWST MIRI data for a range of irradiation conditions and atmospheric compositions. To do this, we adapt the GENESIS self-consistent atmospheric model (Gandhi & Madhusudhan 2017; Piette et al. 2020; Piette & Madhusudhan 2020a) for non- H_2 rich compositions. We first test the case of Trappist-1 b assuming a Venus-like composition and find that ~ 30 secondary eclipses with MIRI LRS result in a confident CO_2 detection, consistent with previous studies (Lustig-Yaeger et al. 2019). The retrieval framework is able to accurately constrain the atmospheric chemical composition and temperature profile to within 2σ , validating the method.

We then identify optimal rocky exoplanet candidates for atmospheric characterisation with JWST using a simple observability metric. The mid-infrared is an ideal spectral range for such efforts given the abundance of molecular features in this range and the relatively higher signal-to-noise ratio (S/N) in secondary eclipse. We therefore rank the observability of known rocky exoplanets by considering the number of eclipses required with MIRI LRS to detect the thermal emission spectrum at $S/N=3$ at a resolution of $R \sim 10$, $E_{S/N=3}$. This resolution is chosen to provide a metric for the spectroscopic observability of rocky exoplanets, which is relevant for the chemical characterisation of their atmospheres. As expected, host star brightness, planetary radius and planetary temperature play key roles in determining observability. While brighter host stars result in smaller observational uncertainties, larger planetary radii and temperatures result in a greater signal for a given stellar radius and temperature.

We find that > 30 known rocky exoplanets should have detectable thermal emission signatures with MIRI LRS at $S/N=3$ and a resolution of $R \sim 10$. Of these, 14 are more observable than GJ 1132 b, which is considered to be an optimal target for rocky exoplanet atmospheric characterisation (Morley et al. 2017). In particular, we find that LHS 3844 b, GJ 1132 b and Trappist-1 b each represent ideal candidates for the hot (~ 1000 K), warm (~ 600 K) and temperate (~ 300 – 400 K) regimes, respectively. We therefore focus on these case studies to assess the observability of secondary atmospheres across this range of irradiation conditions.

We investigate the observational strategies required to characterise a range of CO_2 -rich to H_2O -rich atmospheres in LHS 3844 b, GJ 1132 b and Trappist-1 b. In particular, we consider four key

science cases in order of scientific complexity which may be addressed by thermal emission observations of these atmospheres: (i) Is the spectrum consistent with a hot, bare rock surface (assuming no heat redistribution, as investigated by Koll et al. 2019)? (ii) Are spectral features detected in the spectrum, confirming atmospheric absorption? i.e. Can a blackbody be ruled out by the data? (iii) Is CO₂ confidently detected in the spectrum, e.g. using the prominent spectral feature at $\sim 9 \mu\text{m}$? (iv) Is H₂O confidently detected?

We investigate the confidence with which these science cases can be addressed for a cloud-free Venus-like (CO₂-rich), 50% CO₂/50% H₂O or 100% H₂O atmosphere for the case studies LHS 3844 b, GJ 1132 b and Trappist-1 b. For LHS 3844 b, we find that 8 MIRI LRS eclipses are sufficient to confidently characterise a cloud-free Venus-like composition, leading to $> 4\sigma$ detections of CO₂ and H₂O. Alternatively, 20 eclipses with MIRI LRS allow both a Venus-like and 50% CO₂/50% H₂O composition to be confidently characterised, while a blackbody spectrum would be significantly rejected (at $> 4\sigma$) in the case of a 100% H₂O composition, indicating atmospheric absorption. Furthermore, in the cases where CO₂ and H₂O are detected, their abundances can be constrained within ~ 0.5 dex, i.e. comparable to the precision currently achieved for hot Jupiters (e.g. Sheppard et al. 2017; Welbanks et al. 2019).

For GJ 1132 b, we find that 8 eclipses with MIRI LRS allow $> 4\sigma$ detections of CO₂ and H₂O for the Venus-like composition, and can rule out a blackbody spectrum at $\sim 4\sigma$ for a 100% H₂O composition. Meanwhile, a longer observing time strategy of 20 MIRI LRS eclipses allows $> 3\sigma$ detections of CO₂ and H₂O across the CO₂-to H₂O-dominated compositions considered here. Furthermore, in the cases where CO₂ and H₂O are detected, their abundances are constrained to within 1σ uncertainties of $\lesssim 0.75$ dex.

In the case of Trappist-1 b, we find that a Venus-like composition could be readily characterised with 30 MIRI LRS eclipses, consistent with previous studies (Lustig-Yaeger et al. 2019). In particular, we find that $\sim 5\sigma$ detections of CO₂ and H₂O would be possible for a Venus-like composition and that, in the case of a 50% CO₂/50% H₂O composition, H₂O could be detected at $\sim 3\sigma$. We also consider a longer observing time strategy of 80 eclipses with MIRI LRS, and find that this leads to $> 4\sigma$ detections of CO₂ and H₂O across the Venus-like and 50% CO₂/50% H₂O compositions, while a blackbody spectrum is rejected at $> 4\sigma$ in the case of a 100% H₂O composition. For both of these observing strategies, the abundances of CO₂ and H₂O (in the cases where they are detected) are constrained to within a $1-\sigma$ precision of < 0.7 dex. In addition to the chemical constraints described above, we find that the photospheric temperature profiles of LHS 3844 b, GJ 1132 b and Trappist-1 b are all accurately retrieved within the 2σ uncertainties, with temperature constraints as tight as ~ 100 K in some cases. The observing strategies described above for each of these planets may therefore provide an unprecedented view into the thermal conditions on these rocky worlds.

We also find that for the longer observing time strategies investigated here, an additional 4 eclipses with the F1500W photometry band do not contribute significantly to the constraints achieved with the MIRI LRS data alone. The degeneracies between opacity from different molecules such as CO₂ and H₂O make it challenging to place chemical constraints on the atmosphere using photometry. For example, while the F1500W bandpass probes a strong CO₂ feature, it is also impacted by a broad, continuum feature of H₂O. Therefore, a MIRI LRS-only observing strategy may be ideal for the initial chemical characterisation of rocky exoplanets. However, mid-infrared photometric observations are valuable as quick tests for the presence of an atmosphere as they are able to distinguish scenarios with/without

atmospheric energy redistribution (Koll et al. 2019, see also Figure 5).

The temperature profiles we explore in this work are for clear atmospheres, though we note that clouds and hazes may affect the temperature profile and resulting thermal emission spectrum. For example, optical scattering from clouds and hazes can result in somewhat muted spectral features (e.g. Morley et al. 2015; Piette & Madhusudhan 2020a). For the case studies LHS 3844 b, GJ 1132 b and Trappist-1 b, we find that photospheric temperatures could nevertheless be measured with MIRI LRS and/or MIRI photometry in the case of a high, Venus-like Bond albedo of 0.7. Such a measurement would allow joint constraints on the Bond albedo and energy redistribution efficiency in the atmosphere, and very cool photospheric temperatures (i.e. high Bond albedos) may suggest the presence of clouds. Thermal emission observations will therefore provide a unique opportunity to probe the conditions in cloudy, rocky exoplanet atmospheres.

The characterisation of rocky exoplanet atmospheres arguably represents the next frontier in exoplanet science. We have shown here that secondary eclipse observations with JWST/MIRI will be able to place important constraints on atmospheric chemistry of rocky exoplanets and potential geochemical signatures. Furthermore, we find that > 30 known rocky exoplanets are suitable candidates for dayside atmospheric characterisation with JWST/MIRI. Thermal emission spectroscopy offers an unparalleled opportunity to characterise secondary atmospheres, whose small scale heights can be prohibitive in transmission spectroscopy, and will be an essential tool to characterise exo-geology in the near future.

ACKNOWLEDGEMENTS

We thank the anonymous reviewer for their thorough and helpful comments on our manuscript. We also thank Subhajit Sarkar for help with validating our PandExo uncertainties against JexoSim. AAAP acknowledges support from the UK Science and Technology Facilities Council (STFC) towards her doctoral studies. This research has made use of the NASA Exoplanet Archive, which is operated by the California Institute of Technology, under contract with the National Aeronautics and Space Administration under the Exoplanet Exploration Program.

DATA AVAILABILITY

No new data were generated or analysed in support of this research.

REFERENCES

- Almenara J. M., Díaz R. F., Bonfils X., Udry S., 2016, *A&A*, **595**, L5
- Angelo I., Hu R., 2017, *AJ*, **154**, 232
- Astudillo-Defru N., et al., 2020, *A&A*, **636**, A58
- Barklem P. S., Collet R., 2016, *A&A*, **588**, A96
- Barragán O., et al., 2018, *A&A*, **612**, A95
- Barros S. C. C., et al., 2014, *A&A*, **569**, A74
- Barstow J. K., Aigrain S., Irwin P. G. J., Kendrew S., Fletcher L. N., 2015, *MNRAS*, **448**, 2546
- Batalha N. E., et al., 2017, *PASP*, **129**, 064501
- Benneke B., Seager S., 2012, *ApJ*, **753**, 100
- Benneke B., Seager S., 2013, *ApJ*, **778**, 153
- Berta-Thompson Z. K., et al., 2015, *Nature*, **527**, 204
- Bonfils X., et al., 2018, *A&A*, **618**, A142
- Bourrier V., et al., 2017, *A&A*, **599**, L3

- Buchner J., et al., 2014, *A&A*, **564**, A125
- Burrows A., Budaj J., Hubeny I., 2008, *ApJ*, **678**, 1436
- Castelli F., Kurucz R. L., 2003, in Piskunov N., Weiss W. W., Gray D. F., eds, IAU Symposium Vol. 210, Modelling of Stellar Atmospheres. p. A20 ([arXiv:astro-ph/0405087](https://arxiv.org/abs/astro-ph/0405087))
- Castor J. I., Dykema P. G., Klein R. I., 1992, *ApJ*, **387**, 561
- Christiansen J. L., et al., 2017, *AJ*, **154**, 122
- Cloutier R., et al., 2019, *A&A*, **629**, A111
- Cloutier R., et al., 2020a, *AJ*, **160**, 3
- Cloutier R., et al., 2020b, *AJ*, **160**, 22
- Crossfield I. J. M., 2015, *PASP*, **127**, 941
- Cubillos P. E., et al., 2021, *ApJ*, **915**, 45
- Cutri R. M., et al., 2003, 2MASS All Sky Catalog of point sources.
- Dai F., Masuda K., Winn J. N., Zeng L., 2019, *ApJ*, **883**, 79
- Damasso M., et al., 2019, *A&A*, **624**, A38
- Davies J. H., Davies D. R., 2010, *Solid Earth*, **1**, 5
- Deming D., et al., 2009, *PASP*, **121**, 952
- Demory B.-O., et al., 2016, *Nature*, **532**, 207
- Diamond-Lowe H., Berta-Thompson Z., Charbonneau D., Kempton E. M. R., 2018, *AJ*, **156**, 42
- Diamond-Lowe H., Charbonneau D., Malik M., Kempton E. M. R., Beletsky Y., 2020, *AJ*, **160**, 188
- Dorn C., Noack L., Rozel A. B., 2018, *A&A*, **614**, A18
- Dressing C. D., et al., 2015, *ApJ*, **800**, 135
- Dumusque X., et al., 2019, *A&A*, **627**, A43
- Elkins-Tanton L. T., Seager S., 2008, *ApJ*, **685**, 1237
- Espinoza N., et al., 2020, *MNRAS*, **491**, 2982
- Feautrier P., 1964, *Comptes Rendus Academie des Sciences (serie non spec- ifiee)*, **258**, 3189
- Feng Y. K., Line M. R., Fortney J. J., Stevenson K. B., Bean J., Kreidberg L., Parmentier V., 2016, *ApJ*, **829**, 52
- Feng Y. K., Line M. R., Fortney J. J., 2020, *AJ*, **160**, 137
- Feroz F., Hobson M. P., Bridges M., 2009, *MNRAS*, **398**, 1601
- Fortney J., et al., 2019, Astro2020: Decadal Survey on Astronomy and As- trophysics, **2020**, 146
- Fridlund M., et al., 2017, *A&A*, **604**, A16
- Frustagli G., et al., 2020, *A&A*, **633**, A133
- Gaia Collaboration et al., 2018, *A&A*, **616**, A1
- Gaillard F., Scaillet B., 2014, *Earth and Planetary Science Letters*, **403**, 307
- Gandhi S., Madhusudhan N., 2017, *MNRAS*, **472**, 2334
- Gandhi S., Madhusudhan N., 2018, *MNRAS*, **474**, 271
- Gandhi S., Madhusudhan N., Hawker G., Piette A., 2019, *AJ*, **158**, 228
- Gillon M., et al., 2016, *Nature*, **533**, 221
- Gillon M., et al., 2017a, *Nature Astronomy*, **1**, 0056
- Gillon M., et al., 2017b, *Nature*, **542**, 456
- Glasse A., et al., 2015, *PASP*, **127**, 686
- Greene T. P., Line M. R., Montero C., Fortney J. J., Lustig-Yaeger J., Luther K., 2016, *ApJ*, **817**, 17
- Guenther E. W., et al., 2017, *A&A*, **608**, A93
- Hammond M., Pierrehumbert R. T., 2017, *ApJ*, **849**, 152
- Herbert O., Woitke P., Helling C., Zerkle A., 2020, *A&A*, **636**, A71
- Hu R., Ehlmann B. L., Seager S., 2012, *ApJ*, **752**, 7
- Hu R., Peterson L., Wolf E. T., 2020, *ApJ*, **888**, 122
- Husser T.-O., Wende-von Berg S., Dreizler S., Homeier D., Reinert A., Bar- man T., Hauschildt P. H., 2013, *A&A*, **553**, A6
- Irwin P. G. J., Parmentier V., Taylor J., Barstow J., Aigrain S., Lee E. K. H., Garland R., 2020, *MNRAS*, **493**, 106
- Karman T., et al., 2019, *Icarus*, **328**, 160
- Kempton E. M. R., et al., 2018, *PASP*, **130**, 114401
- Knutson H. A., et al., 2007, *Nature*, **447**, 183
- Koll D. D. B., 2019, arXiv e-prints, p. [arXiv:1907.13145](https://arxiv.org/abs/1907.13145)
- Koll D. D. B., Abbot D. S., 2016, *ApJ*, **825**, 99
- Koll D. D. B., Malik M., Mansfield M., Kempton E. M. R., Kite E., Abbot D., Bean J. L., 2019, *ApJ*, **886**, 140
- Kosiarek M. R., et al., 2019, *AJ*, **157**, 116
- Kreidberg L., 2018, Exoplanet Atmosphere Measurements from Transmis- sion Spectroscopy and Other Planet Star Combined Light Observations. p. 100, [doi:10.1007/978-3-319-55333-7_100](https://doi.org/10.1007/978-3-319-55333-7_100)
- Kreidberg L., et al., 2019, *Nature*, **573**, 87
- Kurucz R. L., 1979, *ApJS*, **40**, 1
- Lam K. W. F., et al., 2018, *A&A*, **620**, A77
- Lavie B., et al., 2017, *AJ*, **154**, 91
- Leconte J., Forget F., Lammer H., 2015, *Experimental Astronomy*, **40**, 449
- Lee J. M., Fletcher L. N., Irwin P. G. J., 2012, *MNRAS*, **420**, 170
- Lichtenberg T., 2021, *ApJ*, **914**, L4
- Line M. R., et al., 2013, *ApJ*, **775**, 137
- López-Morales M., et al., 2016, *AJ*, **152**, 204
- Luque R., et al., 2019, *A&A*, **628**, A39
- Lustig-Yaeger J., Meadows V. S., Lincowski A. P., 2019, *AJ*, **158**, 27
- Madhusudhan N., 2018, Atmospheric Retrieval of Exoplanets. p. 104, [doi:10.1007/978-3-319-55333-7_104](https://doi.org/10.1007/978-3-319-55333-7_104)
- Madhusudhan N., 2019, *ARA&A*, **57**, 617
- Madhusudhan N., Seager S., 2009, *ApJ*, **707**, 24
- Madhusudhan N., Seager S., 2010, *ApJ*, **725**, 261
- Madhusudhan N., Lee K. K. M., Mousis O., 2012, *ApJ*, **759**, L40
- Malik M., Kempton E. M. R., Koll D. D. B., Mansfield M., Bean J. L., Kite E., 2019, *ApJ*, **886**, 142
- Mansfield M., Kite E. S., Hu R., Koll D. D. B., Malik M., Bean J. L., Kempton E. M. R., 2019, *ApJ*, **886**, 141
- Ment K., et al., 2019, *AJ*, **157**, 32
- Mollière P., Wardenier J. P., van Boekel R., Henning T., Molaverdikhani K., Snellen I. A. G., 2019, *A&A*, **627**, A67
- Moran S. E., Hörst S. M., Batalha N. E., Lewis N. K., Wakeford H. R., 2018, *AJ*, **156**, 252
- Morley C. V., Fortney J. J., Marley M. S., Zahnle K., Line M., Kempton E., Lewis N., Cahoy K., 2015, *ApJ*, **815**, 110
- Morley C. V., Kreidberg L., Rustamkulov Z., Robinson T., Fortney J. J., 2017, *ApJ*, **850**, 121
- Moses J. I., 2014, *Philosophical Transactions of the Royal Society of London Series A*, **372**, 20130073
- Mugnai L. V., et al., 2021, *AJ*, **161**, 284
- Parro L. M., Jiménez-Díaz A., Mansilla F., Ruiz J., 2017, *Scientific Reports*, **7**, 45629
- Pawlowsky-Glahn V., Egozcue J. J., 2006, *Geological Society of London Special Publications*, **264**, 1
- Persson C. M., et al., 2018, *A&A*, **618**, A33
- Piette A. A. A., Madhusudhan N., 2020a, arXiv e-prints, p. [arXiv:2009.11290](https://arxiv.org/abs/2009.11290)
- Piette A. A. A., Madhusudhan N., 2020b, *MNRAS*, **497**, 5136
- Piette A. A. A., Madhusudhan N., McKemmish L. K., Gandhi S., Masseron T., Welbanks L., 2020, *MNRAS*, **496**, 3870
- Rice K., et al., 2019, *MNRAS*, **484**, 3731
- Richard C., et al., 2012, *Journal of Quantitative Spectroscopy and Radiative Transfer*, **113**, 1276
- Rothman L. S., et al., 2010, *J. Quant. Spectrosc. Radiative Transfer*, **111**, 2139
- Rothman L. S., et al., 2013, *J. Quant. Spectrosc. Radiative Transfer*, **130**, 4
- Santerne A., et al., 2018, *Nature Astronomy*, **2**, 393
- Scheucher M., et al., 2020, *ApJ*, **898**, 44
- Schlichting H. E., Young E. D., 2021, arXiv e-prints, p. [arXiv:2107.10405](https://arxiv.org/abs/2107.10405)
- Sheppard K. B., Mandell A. M., Tamburo P., Gandhi S., Pinhas A., Mad- husudhan N., Deming D., 2017, *ApJ*, **850**, L32
- Showman A. P., Fortney J. J., Lian Y., Marley M. S., Freedman R. S., Knutson H. A., Charbonneau D., 2009, *ApJ*, **699**, 564
- Shporer A., et al., 2020, *ApJ*, **890**, L7
- Skilling J., 2006, *Bayesian Anal.*, **1**, 833
- Skrutskie M. F., et al., 2006, *AJ*, **131**, 1163
- Southworth J., Mancini L., Madhusudhan N., Mollière P., Cicci S., Henning T., 2017, *AJ*, **153**, 191
- Stassun K. G., et al., 2019, *AJ*, **158**, 138
- Swain M. R., et al., 2021, *AJ*, **161**, 213
- Taylor J., Parmentier V., Irwin P. G. J., Aigrain S., Lee E. K. H., Krissansen- Totton J., 2020, *MNRAS*, **493**, 4342
- Thompson M. A., Telus M., Schaefer L., Fortney J. J., Joshi T., Lederman D., 2021, *Nature Astronomy*, **5**, 575
- Trotta R., 2008, *Contemporary Physics*, **49**, 71
- Tsiaras A., et al., 2016, *ApJ*, **820**, 99

- Turbet M., Bolmont E., Bourrier V., Demory B.-O., Leconte J., Owen J., Wolf E. T., 2020, *Space Sci. Rev.*, **216**, 100
- Vanderspek R., et al., 2019, *ApJ*, **871**, L24
- Waldmann I. P., Rocchetto M., Tinetti G., Barton E. J., Yurchenko S. N., Tennyson J., 2015, *ApJ*, **813**, 13
- Weiss L. M., et al., 2016, *ApJ*, **819**, 83
- Welbanks L., Madhusudhan N., 2021, *ApJ*, **913**, 114
- Welbanks L., Madhusudhan N., Allard N. F., Hubeny I., Spiegelman F., Leininger T., 2019, *ApJ*, **887**, L20
- Western C. M., Carter-Blatchford L., Crozet P., Ross A. J., Morville J., Tokaryk D. W., 2018, *J. Quant. Spectrosc. Radiative Transfer*, **219**, 127
- Winters J. G., et al., 2019, *AJ*, **158**, 152
- Wunderlich F., Scheucher M., Grenfell J. L., Schreier F., Sousa-Silva C., Godolt M., Rauer H., 2021, *A&A*, **647**, A48
- Yu X., Moses J. I., Fortney J. J., Zhang X., 2021, *ApJ*, **914**, 38
- Yurchenko S. N., Tennyson J., 2014, *MNRAS*, **440**, 1649
- Yurchenko S. N., Tennyson J., Barber R. J., Thiel W., 2013, *Journal of Molecular Spectroscopy*, **291**, 69
- Zharkov V. N., 1983, *Moon and Planets*, **29**, 139
- de Wit J., et al., 2016, *Nature*, **537**, 69
- de Wit J., et al., 2018, *Nature Astronomy*, **2**, 214

APPENDIX A: RETRIEVAL WITH HIGHER SURFACE PRESSURE

Figure A1 shows the results of a retrieval for Trappist-1 b similar to that in Section 2.3, but assuming a surface pressure of 100 bar rather than 10 bar in the retrieval model. Both of these surface pressures are deeper than the photosphere and the resulting spectra are therefore not sensitive to the surface pressure. This is demonstrated by the fact that the retrieved atmospheric properties in Figure A1 are the same as those in Figure 3, despite the difference in the surface pressure assumed for the retrieval model.

APPENDIX B: MARGINALISED POSTERIOR PROBABILITY DISTRIBUTIONS FOR MOLECULAR ABUNDANCES

Figure B1 shows the 1D and 2D marginalised posterior probability distributions of the retrieved chemical abundances for the validation retrieval of Trappist-1 b discussed in Section 2.3.

APPENDIX C: OPTIMAL TARGETS FOR ROCKY EXOPLANET THERMAL EMISSION

In Table C1, we list the known rocky exoplanets whose thermal emission in secondary eclipse can be observed to S/N=3 in fewer than 10 eclipses at $R \sim 10$. We have explored the potential for atmospheric characterisation of LHS 3844 b and GJ 1132 b in Section 4 and found that as few as 8 MIRI LRS eclipses are sufficient to detect species such as CO₂ and H₂O depending on the composition of the atmosphere. This list of promising targets therefore represents a population of rocky exoplanets whose atmospheres may be readily characterised in thermal emission using JWST MIRI.

This paper has been typeset from a \LaTeX file prepared by the author.

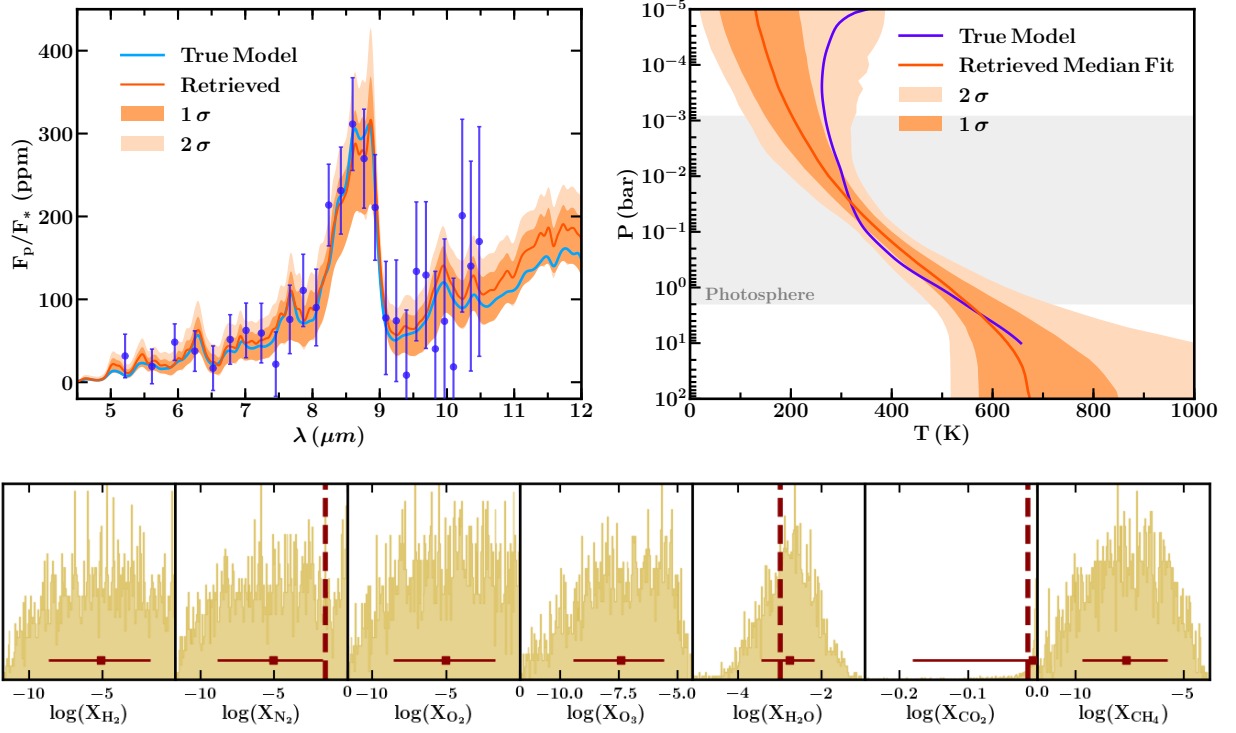


Figure A1. Same as Figure 3 but assuming a surface pressure of 100 bar for the retrieval model, rather than 10 bar. The simulated data is identical to that used in Figure 3. The retrieved atmospheric properties are not sensitive to the difference in surface pressure used in the retrieval model.

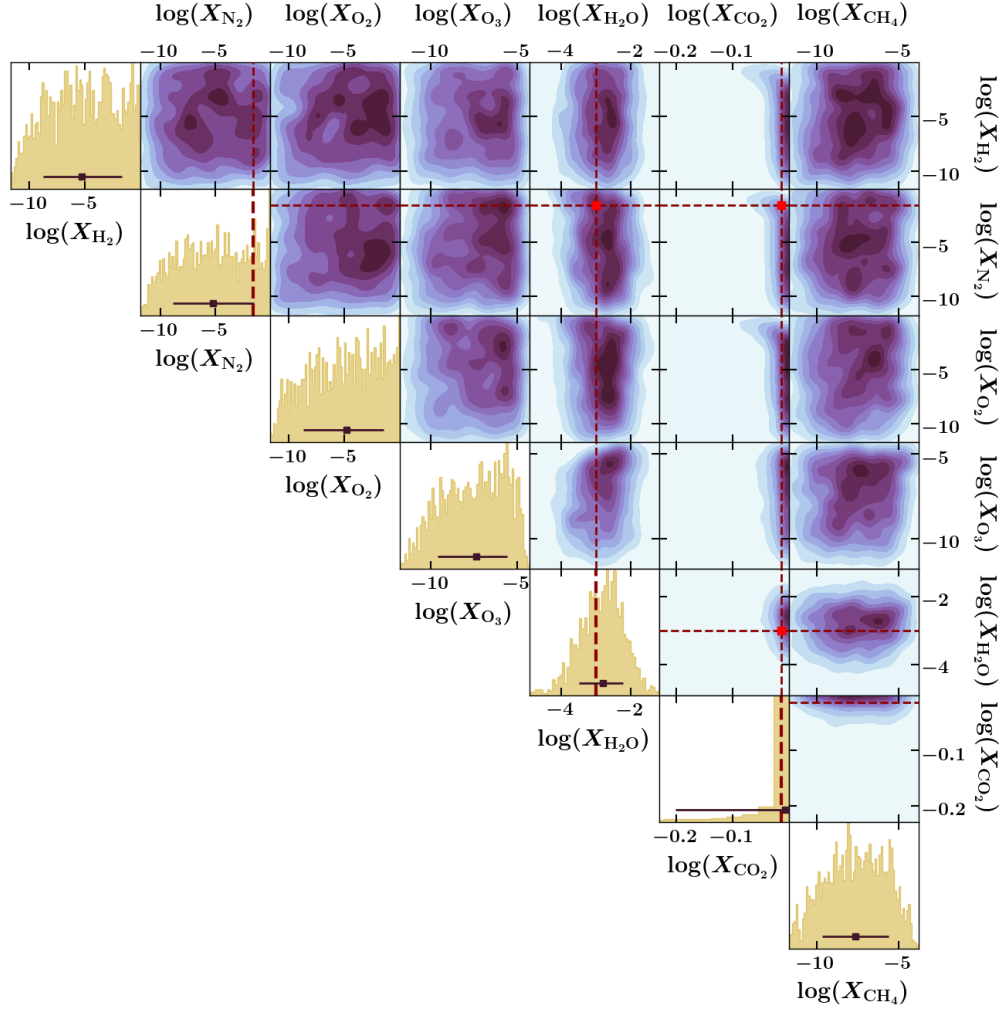


Figure B1. 1D and 2D posterior probability distributions corresponding to the validation retrieval shown in Section 2.3 and Figure 3. The diagonal shows the 1D marginalised posterior probability distributions for each molecular abundance, while off-diagonal panels show 2D marginalised posterior probability distributions. Red squares and dashed lines indicate the true input abundances of CO_2 , N_2 and H_2O . Dark brown squares and error bars show the median and 1-sigma uncertainties in the retrieved abundances.

[htbp]

Table C1. Properties of known rocky exoplanets whose thermal emission in secondary eclipse can be measured to S/N=3 (at $R \sim 10$) in ≤ 10 eclipses with MIRI LRS (see Section 3), listed in order of observability. Note that we do not include 55 Cnc e in this list as it would saturate part of the MIRI LRS detector.

Planet	$R_p (R_\oplus)$	$T_{eq} (K)$	$R_s (R_\odot)$	$T_{eff} (K)$	K mag	Eclipses for S/N=3	Refs
LHS 3844 b	1.30	809	0.19	3036	9.14	0.16	1,2
HD 3167 b	1.70	1752	0.86	5261	7.07	0.17	1,3
HD 219134 b	1.60	1020	0.78	4699	3.26	0.17	1,4
K2-141 b	1.54	2046	0.67	4373	8.40	0.19	1,5
GJ 9827 b	1.58	1186	0.60	4340	7.19	0.26	1,6
HD 213885 b	1.75	2138	1.10	5978	6.42	0.28	1,7
GJ 1252 b	1.19	1091	0.39	3458	7.92	0.29	1,8
LTT 3780 b	1.33	891	0.37	3331	8.20	0.48	1,9
HD 219134 c	1.51	786	0.78	4699	3.26	0.55	1,4
HD 80653 b	1.61	2421	1.22	5838	8.02	0.59	1,10,11
Kepler-21 b	1.64	2034	1.90	6305	6.95	0.73	1, 12
L 168-9 b	1.39	985	0.60	3800	7.08	0.97	1,13
HD 15337 b	1.70	993	0.84	5131	7.04	1.23	1,14
GJ 1132 b	1.13	586	0.21	3270	8.32	1.32	1,15
GJ 357 b	1.22	528	0.34	3505	6.47	1.64	1,16
K2-291 b	1.59	1403	0.90	5520	8.35	1.85	1,17
L 98-59 c	1.35	516	0.31	3412	7.10	2.20	1,18
TOI-1235 b	1.74	758	0.63	3872	7.89	2.47	1,19
LTT 1445 A b	1.38	438	0.28	3337	6.50	2.59	1,20
Kepler-10 b	1.47	2190	1.06	5708	9.50	2.74	1,21
WASP-47 e	1.82	2209	1.16	5576	10.19	3.25	1,22
GJ 9827 c	1.24	821	0.60	4340	7.19	3.54	1,6
CoRoT-7 b	1.58	1766	0.82	5259	9.81	3.85	1,23,24
K2-265 b	1.71	1427	0.98	5477	9.26	3.87	1,25
K2-229 b	1.16	1964	0.79	5185	9.05	3.94	1,26
Kepler-93 b	1.48	1140	0.92	5655	8.37	4.13	1,27,28
EPIC 220674823 b	1.52	2291	0.87	5470	10.34	4.14	1,29
K2-216 b	1.75	1104	0.72	4503	9.72	4.43	1,30
K2-111 b	1.90	1233	1.23	5730	9.38	5.69	1,31
K2-36 b	1.43	1351	0.72	4916	9.45	5.79	1,32
LHS 1140 c	1.28	436	0.21	3216	8.82	9.73	1,33
L 98-59 d	1.57	408	0.31	3412	7.10	9.84	1,18

Values obtained from: 1. [Skrutskie et al. \(2006\)](#), 2. [Vanderspek et al. \(2019\)](#), 3. [Christiansen et al. \(2017\)](#), 4. [Gillon et al. \(2017a\)](#), 5. [Barragán et al. \(2018\)](#), 6. [Rice et al. \(2019\)](#), 7. [Espinoza et al. \(2020\)](#), 8. [Shporer et al. \(2020\)](#), 9. [Cloutier et al. \(2020a\)](#), 10. [Frustagli et al. \(2020\)](#), 11. [Gaia Collaboration et al. \(2018\)](#), 12. [López-Morales et al. \(2016\)](#), 13. [Astudillo-Defru et al. \(2020\)](#), 14. [Dumusque et al. \(2019\)](#), 15. [Bonfils et al. \(2018\)](#), 16. [Luque et al. \(2019\)](#), 17. [Kosiarek et al. \(2019\)](#), 18. [Cloutier et al. \(2019\)](#), 19. [Cloutier et al. \(2020b\)](#), 20. [Winters et al. \(2019\)](#), 21. [Weiss et al. \(2016\)](#), 22. [Almenara et al. \(2016\)](#), 23. [Barros et al. \(2014\)](#), 24. [Dai et al. \(2019\)](#), 25. [Lam et al. \(2018\)](#), 26. [Santerne et al. \(2018\)](#), 27. [Dressing et al. \(2015\)](#), 28. [Stassun et al. \(2019\)](#), 29. [Guenther et al. \(2017\)](#), 30. [Persson et al. \(2018\)](#), 31. [Fridlund et al. \(2017\)](#), 32. [Damasso et al. \(2019\)](#), 33. [Ment et al. \(2019\)](#).